IMMUNE ORGANOIDS TO STUDY ANTIGEN PRESENTATION

A Dissertation

Presented to the Faculty of the Graduate School

of Cornell University

In Partial Fulfillment of the Requirements for the Degree of

Doctor of Philosophy

by

Kristine Lai

December 2021

IMMUNE ORGANOIDS TO STUDY ANTIGEN PRESENTATION

Kristine Lai

Cornell University 2021

Vaccine and immunotherapy development needs to be timely to provide treatments for infections and cancer. Current platforms for testing vaccines and immunotherapies are limited to cell cultures with little physiological relevance or animal models that have species-specific responses. Likewise, cancer drugs and signaling pathways are evaluated in cell cultures without key environmental cues or stromal support. To address these limitations, we developed immune organoids that recapitulate aspects of lymph nodes and spleen to study antigen presentation in immune tissues and drug response of malignant immune cells. We highlighted existing immune organoid models and vaccine adjuvants (Chapter 1). To investigate materials suitable for immune organoids, we compared the effect of PEG endpoint chemistry and mechanoreceptor integrin ligands on B cell maturation (Chapter 2). Incorporating immune organoids in models of malignant immune cells, we showed that lymphomas were susceptible to drugs in an extracellular matrix and stromal cell-dependent manner (Chapter 3). To study the mode of antigen presentation, we engineered and compared cell-based and artificial polymeric bead-based antigen presenting cells (Chapter 4). Inspired by the particle-based presentation of protein antigens, we developed an immunomodulatory nanogel that enhance immune response in animal models and immune organoids. Finally, we presented potential ideas to further improve of immune organoids (Chapter 5). In the long term, immune organoids can be used to develop vaccines and immunotherapies.

BIOGRAPHICAL SKETCH

Kristine Lai grew up in southern California. She graduated with a B.S. in Mechanical Engineering with High Honors from University of California, Santa Barbara. She received multiple scholarships for her academic merit, including the Northrop Grumman Scholarship and William R. Hearst Scholarship. As an undergraduate researcher under the guidance of Dr. Carl Meinhart and Dr. Martin Moskovits, she used microfluidic devices and Raman spectroscopy to detect opiate derivatives, and was published in Analytical Chemistry. For her presentation of her work, she received an Outstanding Poster Presentation Award at the 2015 SACNAS Conference. She began her graduate work at Cornell University in the Mechanical Engineering Ph.D. program. She studied polymer materials for immune organoids and lymphoma organoids. She also characterized poly(2-hydroxyethyl methacrylate)-pyridine self-assembly nanogels in animal models and immune organoids. Her contributions to these projects have been published in Science Advances, Advanced Functional Materials, and Nature Immunology. She was awarded a Nanotechnology and Nanodelivery focus group award at the Controlled Release Society Annual Meeting in 2020.

For my parents

ACKNOWLEDGMENTS

Firstly, I would like to thank my advisor, Dr. Ankur Singh, for mentoring me during my Ph.D. program. He always took time to help with troubleshooting experiments and analyzing data. I am grateful for my committee members, Dr. Brian Kirby and Dr. Chris Xu, for sharing expertise in their fields. I learned so much from each of my fellow lab members at Cornell, Dr. Shivem Shah, Dr. Sungwoong Kim, Dr. Pamela Graney, Dr. Matthew Mosquera, Dr. Jessica Elmore, Dr. Alberto Purwada, Dr. FNU Apoorva, Monica Zhong, Tibra Wheeler, Regan Stephenson and Vincent Fan. Dr. Paula Miller from the neighboring lab space was a huge help with lab and building logistics. Lyn Park made ordering for items for my projects seamless, and I am grateful for her timely work which enabled the research. I am thankful that my fellow lab members at Georgia Tech were welcoming when I arrived in Atlanta for the last few months of my program. Working with my collaborators, Dr. Ty Moeller, Dr. Matthew DeLisa, and Dr. Kibaek Choe, has been a privilege. I was able to participate in outstanding studies and broaden my scope because of them. I would like to thank my undergraduate research mentees, Pooja Reddy, Mariya Tasnim, and Halee Kim, for their contributions and friendship. My friends in Cornell Mechanical and Aerospace Engineering and Dr. Marcia Sawyer made it a joy to be a part of the Cornell graduate community. My teammates and coach on the Cornell Sport Taekwondo team showed me that I can do more than I ever imagined. Finally, I am deeply grateful for the support of my family. My partner brightens each day and encourages me in all that I do. My sisters share great advice and wisdom with me when I need moral support. My parents inspire me with their accomplishments and cheer me on in all my pursuits. Thank you for your love, sacrifice, and support.

TABLE OF CONTENTS

LIST OF FIGURES

LIST OF ABBREVIATIONS

ECM	Extracellular matrix
GC	Germinal center
BCR	B cell receptor
FDC	Follicular dendritic cell
DLBCL	Diffuse large B cell lymphoma
VCAM-1	Vascular cell adhesion molecule 1
ICAM-1	Intercellular cell adhesion molecule 1
CD40L	Cluster of differentiation 40 ligand
BAFF	B cell activating factor of the tumor necrosis factor family
PEG	Poly(ethylene glycol)
NHS	N-Hydroxysuccinimide
UV	Ultraviolet
MAL	Maleimide
VS	Vinylsulfone
ACR	Acrylate
PEG-4MAL	Poly(ethylene glycol) with 4 maleimide arms
PEG-4VS	Poly(ethylene glycol) with 4 vinylsulfone arms
PEG-4ACR	Poly(ethylene glycol) with 4 acrylate arms
MMP	Matrix metalloproteinase
VPM	GCRDVPMSMRGGDRCG peptide
DTT	Dithiothreitol
REDV	GREDVGC peptide
GFOGER	GGYGGGP$(GPP)_5$GFOGER$(GPP)_5$GPC peptide
RDG	GRDGSPC
WT	Wild-type
TME	Tumor microenvironment
CBM	CARD11-BCL10-MALT1
BCL10	B-cell lymphoma/leukemia 10
MALT1	Mucosa-associated lymphoid tissue lymphoma translocation protein 1
ABC-DLBCL	Activated B cell subtype of diffuse large B cell lymphoma
TLR	Toll-like receptor
IKK	IκB kinase
PDX	Patient-derived xenograft
NP-OVA	4-hydroxy-3-nitrophenylacetyl-ovalbumin
EZH2	Enhancer of zeste homolog 2
H3k27me3	Tri-methylation of lysine 27 on histone H3 protein
PLGA	Poly(lactic-co-glycolic acid)
THF	Tetrahdydrofuran
pHEMA	Polyhydroxyethylmethacrylate
DMAP	4-dimethylaminopyridine
DCM	Dichloromethane
HEK	Human embryonic kidney
H3k27me3	Histone 3 lysine 27 trimethylation
PDMS	Polydimethylsiloxane

CXCR4	CXC motif chemokine receptor 4
CXCL12	CXC motif chemokine ligand 12
SDF1	Stromal cell derived factor 1

CHAPTER 1

Antigen Presentation in Models of Immune Tissues

1.1 Abstract

Vaccines and immunotherapy are studied in 2D cell cultures or animal models. However, these methods of evaluating therapeutics have drawbacks. 2D *in vitro* models of immune tissues lack physiological relevance. Biological processes are difficult to decouple in *in vivo* animal models, and species-dependent signaling reduces the relevance of animal models to human responses. This chapter introduces immune organoids and antigen presentation. Immune organoids recapitulate ECM motifs and mechanical cues that 2D cell cultures lack. Polymer endpoint chemistry of immune organoids is discussed in Chapter 2. We explore how immune organoids are used to study B cell malignancies, which are further discussed in Chapter 3. Modes of antigen presentation for immune cell interactions and immunomodulatory nanovaccine delivery are discussed in Chapter 4.

1.2 Introduction

Vaccines are used to teach the immune system how to fight off disease-causing organisms before the body encounters them. The immune system responds to pathogens by an innate immune response, which is the body's first line of defense, and an adaptive immune response, which is slower and learns to target specific pathogens when encountered again. B lymphocytes produce antibodies to neutralize pathogens. Antibodies bind to disease-causing organisms as a part of the adaptive immune response[1] (Figure 1-1A). Antibodies are produced by B lymphocytes, which are produced in primary lymphoid organ bone marrow, and home to secondary lymphoid organs, which include lymph nodes, spleen, and Peyer's patches (Figure 1-1B). Vaccines are used to train

the body to produce antibodies against pathogens such as bacteria and viruses (Figure 1-1C). In a secondary lymphoid organ, B cells encounter antigen and undergo activation by receiving signals from follicular helper T cells (Figure 1-2A). Signals such as CD40L and B-cell activating factor (BAFF) are required for B cell activation and survival. CD40L and T cell receptor on T follicular helper (Tfh) cells bind with CD40 and MHC, respectively, on B cells for B cell activation. BAFF is produced by macrophages, monocytes, and dendritic cells[2].

To produce antibodies with high specificity to an antigen, B cells enter B cell zones within secondary lymphoid organs and form germinal centers (GCs). Germinal centers are organized into dark zones and light zones. GC B cells expressing CXCR4 migrate toward CXCR4 ligand CXCL12 (SDF-1) in dark zones[3]. Within germinal centers dark zones, B cells rapidly proliferate and undergo somatic hypermutation of the variable region genes (Figure 1-2B). Antigen-specific B cell receptors (BCRs) must be selected to neutralize disease causing organisms, so the large number of B cells undergo selection. Follicular dendritic cells (FDCs) present antigen to B cells, and cells with high affinity BCR continue to proliferate and mutate whereas cells with low affinity BCR undergo apoptosis, programmed cell death. After several cycles of proliferation, somatic hypermutation, and selection, B cells undergo class switching to form immunoglobulin isotypes that have improved function for fighting disease-causing organisms. B cells then differentiate into plasma cells, which produce antibodies, or memory B cells, which circulate long term to retain the ability to fight off recurrences of disease-causing organisms by differentiating into plasma cells and producing antibodies. Germinal centers and immunity are generally studied using complex transgenic mouse models.

1.3 Immune Organoid Models of Germinal Centers

Since CD40L signal from T cells is required for B cell activation and germinal formation, cell-based presentation of CD40L[4], or cell-free CD40L[5] have been used to stimulate B cells in *in vitro* models of germinal centers. Fibroblasts transfected with CD40L and BAFF (40LB) induced expansion of GC-like cells *in vitro*[4]. Few primary B cells survive in 2D co-culture[6], so 3D immune organoid models have been developed to more closely mimic *in vivo* conditions and allow for primary B cell survival and proliferation.

Integrin ligands provide ECM signals to immune cells. GC B cells express αvβ3 integrins, which bind to vitronectin protein RGD, and α4β1 integrins, which bind to VCAM-1 mimicking REDV. RGD-functionalized gelatin hydrogels induced rapid proliferation of primary murine B cells, with antibody isotype class-switching[6]. PEG-MAL hydrogel immune organoids allow for enrichment of antigen-specific B cells[7].

1.4 B Cell Malignancies

Mutations in B cells can cause dysregulated proliferation and resistance to cell death, leading to cancerous lymphomas. Lymphomas are a heterogeneous group of cancers that initiate in lymph nodes, and the most common form (~30% of cases) is the aggressive diffuse large B-cell lymphoma (DLBCL) subtype. Despite the heterogeneity of lymphomas, patients are treated uniformly with an initial therapy of rituximab, cyclophosphamide, doxorubicin, vincristine, and prednisone (R-CHOP). Patients with DLBCL treated with R-CHOP have a five-year survival rate as low as 50% due to high chemoresistance. Activated B cell diffuse large B cell lymphoma (ABC-DLBCL) is one of the most drug-resistant DLBCLs. Fluid flow has been shown to upregulate

surface expression of BCRs and integrin receptors in ABC-DLBCLs with CD79A/B mutations or WT BCRs[8].

1.5 Antigen Presentation to Immune Cells

In secondary lymphoid organs, small soluble antigens can diffuse through pores in the subcapsular sinus to activate follicular B cells, but larger antigens are presented to B cells by dendritic cells, macrophages, or follicular dendritic cells (FDCs). FDCs maintain germinal center structure by producing CXC-chemokine ligand 13 (CXCL13), which attracts B cells presenting CXCR5. Within GCs, FDCs present antigen to B cells to select for high affinity B cells in GC light zones. GC B cells used strong myosin II contractility and high pulling forces on the BCR to directly regulate BCR binding to antigen[9]. Human GC B cells use pod-like structures to pull on antigen, where high affinity GC B cells form stable synapses with antigen and low affinity GC B cells have dynamic engagement and disengagement with antigen[10]. B cell contractility contributes to testing antigen affinity by breaking bonds between weakly bonded BCR-antigen and only allowing B cells to internalize antigen with high-affinity bonds[11].

GC B cells require continuous presentation of antigen to undergo affinity maturation. FDCs are difficult to isolate. FDC-like cell line HK was established from human tonsils[12]. HK cells supported B cell proliferation and retained expression of some FDC markers such as CD14, CD40, ICAM-1, and VCAM-1, but lost expression of FDC markers CD19, CD23, CD21, and DRC-1. Another way to present antigen to B cells is engineering artificial cells to use FDC mimics.

Artificial APCs have been produced by coupling a soluble human leukocyte antigen–

immunoglobulin fusion protein (HLA-Ig) and CD28-specific antibody to beads[13]. These artificial APCs were then used to expand antigen-specific cytotoxic T cells.

1.6 Toll-Like Receptors in Immunity

Toll-like receptors (TLRs) are a class of proteins that recognize pathogen-associated molecular patterns (PAMPs) to activate innate immunity[14]. Ten TLRs have been identified in humans, and thirteen TLRs have been identified in mice. TLR5 recognizes bacterial flagellin, and activation of TLR5 activates NFκB and TNF-α production through MyD88[15]. TLR2 recognizes several ligands including molecules with diacyl and triacylglycerol moieties, proteins, and polysaccharides[16]. TLR ligands have been tested *in vitro* and *in vivo*, but there is variation of relevant receptors and downstream signaling among species. Organoids can be used to test species-specific TLR signaling while incorporating 3D environmental cues.

1.7 Nanovaccines and Adjuvants for Immunomodulation

Aged individuals and individuals with underlying health conditions can have poor immune responses to conventional vaccines. Aged individuals had decreases compared to young individuals in TNF-α, IL-6, and/or IL-12 (p40) production in myeloid dendritic cells and in TNF-α and IFN-α production in plasmacytoid dendritic cells in response to TLR1/2, TLR2/6, TLR3, TLR5, and TLR8 engagement in mDCs and TLR7 and TLR9 in pDCs[17]. Older individuals are recommended to receive high dose or adjuvanted influenza vaccines[18]. In healthy individuals and individuals with less robust immune response, vaccine efficacy can be increased by improving trafficking to lymphoid organs and adding adjuvants to stimulate the immune response.

Lymph nodes contain large number of antigen presenting cells such as dendritic cells and

macrophages, therefore delivering vaccines directly to lymph nodes induces stronger immune responses than delivering to peripheral tissues. Vaccine vehicle size, charge, and composition can be tuned to target lymph nodes for higher vaccine efficacy[19].

Nanoparticles have shown promise as vaccine delivery vehicles because their structure and composition were formulated to boost immunogenicity. Self-assembled ferritin based nanoparticle vaccines elicited potent neutralizing antibodies against a broad spectrum of H1N1 viruses[20]. Hemagglutinin-stabilized stem ferritin nanoparticles formed from hemagglutinin A (H1N1 1999) elicited broadly cross-reactive antibodies that completely protected mice and partially protected ferrets against lethal heterosubtypic H5N1 influenza virus challenge[21]. The hemagglutinin stem is highly conserved, unlike the head region, which undergoes antigenic drift. Mice injected with a combination of polyanhydride nanoparticles and a pentablock copolymer-based hydrogel developed high neutralizing antibody titers, reduced viral load upon H5N1 challenge[22]. This combination nanovaccine also induced higher neutralizing antibody titers and reduced viral load against H1N1 influenza A virus in young and aged mice, potentially though enhanced activation of dendritic cells[23].

Adjuvants are also play a key role in improving vaccine efficacy. Adjuvants enhance the immunogenicity of the antigens. The most commonly used adjuvant, aluminum hydroxide (alum), works by releasing uric acid to induce monocyte differentiation into inflammatory dendritic cells[24]. TLR agonist adjuvants activate inflammatory innate immune responses and promote adaptive immunity. TLR agonists have been studied in vaccines for cancer therapy[25–28], anthrax[29], parasitic infections[30,31], bacterial infections[32], and viral infections[33,34]. MPLA (TLR4 agonist) and CpG

(TLR9 agonist) have been loaded onto nanodiscs to treat mice with melanoma[27]. A small molecule TLR7/8 agonist loaded onto a polymer scaffold increased vaccine immunogenicity for inducing antibodies and T cell immunity[35]. These formulations all involve taking a polymer and loading it with TLR agonists to boost immunity. However, a polymer that is itself a TLR agonist has not been used in nanovaccine treatment before. Discovery of materials with endogenous immunostimulatory properties can improve nanovaccine immune response.

1.8 Figures

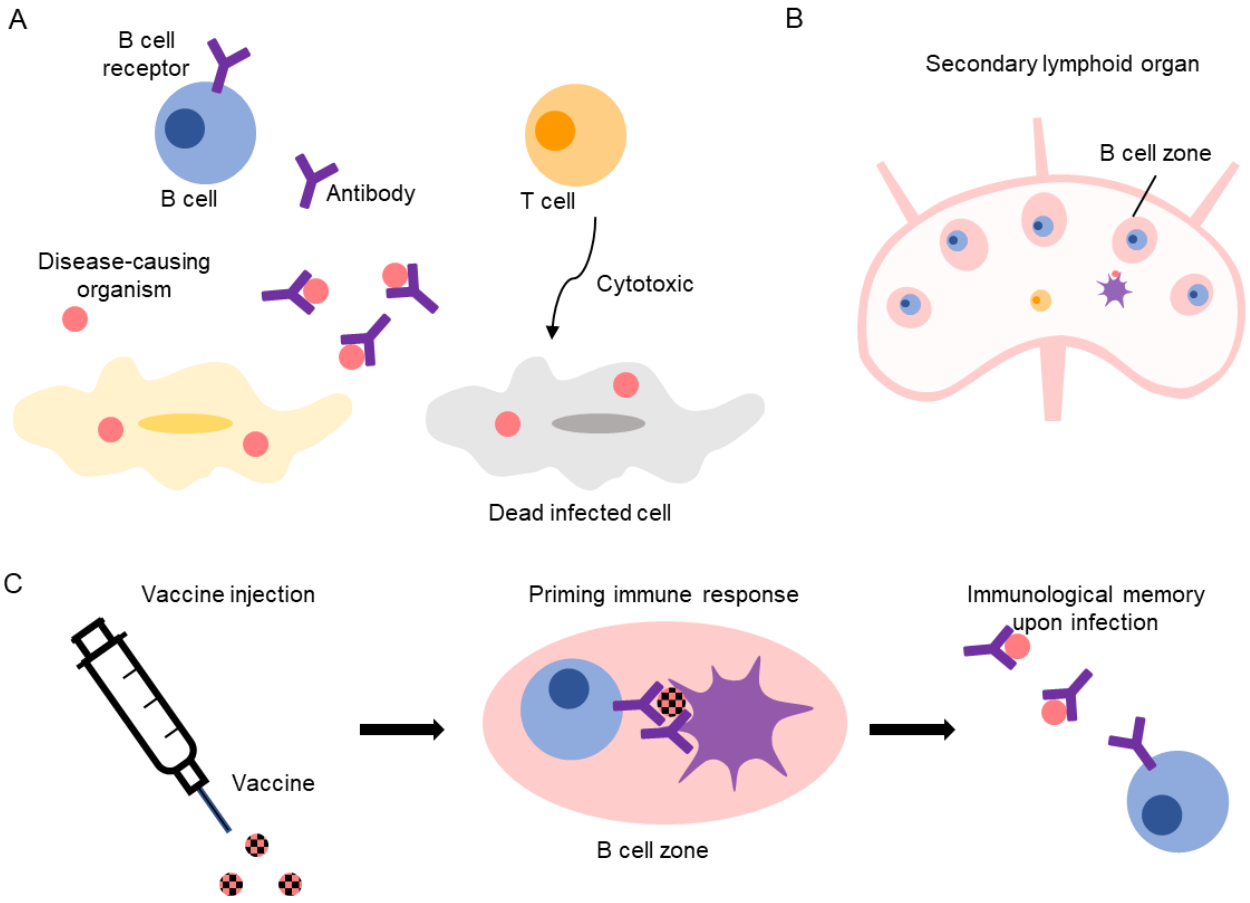

Figure 1-1: Antibodies neutralize disease-causing organisms.

A) B cells respond to pathogens by secreting antibodies to neutralize the antigen. T cells kill infected cells or signal other immune cells to destroy pathogens.

B) Antibodies are produced in secondary lymphoid organs. Within secondary lymphoid organs are B cells zones containing germinal center structures.

C) Vaccines can be used to prime the adaptive immune response to retain immunological memory for disease-causing organisms.

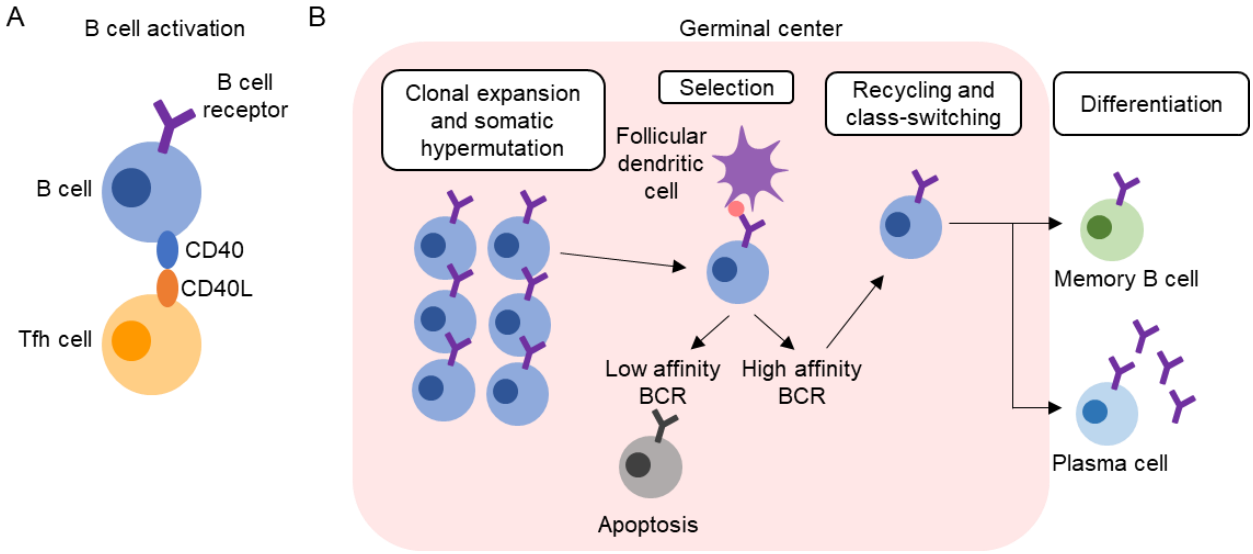

Figure 1-2: B cell activation and germinal center.

A) Naïve B cells encounter Tfh cells to undergo activation.

B) B cells undergo clonal expansion and somatic hypermutation in GC dark zones. B cells migrate to GC light zones, where they undergo selection for high affinity BCRs. After class-switch recombination and recycling between LZ and DZ, GC B cells exit GC and differentiate into memory B cells or plasma cells.

CHAPTER 2

Organoid polymer functionality regulates germinal center response[i]

2.1 Abstract

2D cell culture of B cells with stromal cells does not provide environmental cues to induce *in vivo*-like germinal center response. In this chapter, polyethylene glycol (PEG)-based immune organoids are developed to elucidate the effects of polymer end-point chemistry and integrin ligands on germinal center-like B cell phenotype, to better define the lymph node microenvironment factors regulating *ex vivo* germinal center dynamics. Notably, PEG vinyl sulfone or acrylate fail to sustain primary immune cells, but functionalization with maleimide (PEG-4MAL) leads to B cell expansion and germinal center-like induction. Incorporation of niche-mimicking peptides reveals that collagen-1 promotes germinal center-like dynamics and epigenetics.

2.2 Introduction

Early efforts to elucidate B cell differentiation involved a controlled environment of naïve B cells co-cultured in 2D with stromal cells, called 40LB[4]. These cells were engineered to provide critical signals for B cell survival and differentiation, including the T cell signal CD40L and B cell activating factor (BAFF), secreted in vivo by FDCs. However, the *in vitro* 2D presentation of these signals is not sufficient for the induction of a germinal center response that resembles an *in vivo*-like response[37], suggesting a critical role for the 3D microenvironment. Indeed, we have previously shown that incorporation of naïve murine B cells and 40LB in 3D organoids engineered from gelatin and silicate nanoparticles[6,38] can significantly drive germinal center B cell phenotype, transcriptome, and somatic hypermutation just after 4 days *ex vivo*[37], similar to in vivo immunized

[i] This chapter was published in [123]Graney, Lai et al., *Advanced Functional Materials* 2020

mice. To better decouple the signals driving this response, we further engineered modular organoids with tunable microenvironments using a four-arm polyethylene glycol presenting maleimide (PEG-4MAL) functionalized with thiolated ECM-mimicking peptides and enzymatically degradable crosslinkers[7]. Using this system, we have shown that interactions between integrins and VCAM-1-mimicking peptide regulated phosphorylation of key proteins in murine B cell receptor (BCR) signaling, and demonstrated the ability of immune organoids to generate antigen-specific IgG1 antibodies through the addition of soluble antigen and incorporation of T cell signals, such as Fas ligand[7]. However, to date, the role of PEG end-group chemistry in regulating the germinal center response and contributions of microenvironment-epigenome interactions have not yet been explored, despite that such interactions would be expected to regulate cell behavior. In this chapter we present a direct comparison of PEG endpoint chemistry in the engineering of immune organoids.

2.3 End Group of Hydrogel Macromer and Murine B Cell Survival

To study the effect of various ECM and integrin-binding proteins found in the B cell follicle, we sought to use hydrogel platforms where integrin-binding ligands of interest can be functionalized for presentation to B cells and supporting stromal cells. Although matrices from naturally derived materials have been attempted to build immune tissues, as reviewed by us[39], including our work using a gelatin-based organoid system[6,38], which presented RGD motifs, natural materials do not afford easy control over the microenvironment and presentation of various distinct integrin ligands, may induce confounding effects on immune cell activation due to nonintegrin receptor-ligand interactions, such as CD44 binding in hyaluronic acid-based hydrogels[40], and may suffer from viscosity issues and batch-to-batch variability. Furthermore, we have previously shown that the

photopolymerization of gelatin methacrylate does not generate germinal center response[6,38]. Therefore, we chose to use a milder polymerization reaction that does not require toxic radical photoinitiators for the UV curing. Several alternative chemistries exist for cell encapsulation and cross-linking under physiological conditions, including Schiff-base formation[41,42], amine-NHS ester coupling[43], Diels–Alder reaction[44,45], radical-mediated thiol-ene[46] and thiol-yne[47], and nucleophilic additions of thiols to alkenes or alkyne esters or epoxy groups[48–54]. However, among these, as discussed elsewhere[55], Schiff-base reactions are reversible under physiological conditions and the reaction kinetics of amine-NHS ester, Diels–Alder, chemistries are not highly suitable for homogeneous distribution of cells throughout the hydrogel. In contrast, thiol-based moieties, such as peptides and polymeric macromers, can react with activated alkenes or alkynes using photogenerated radicals (e.g., acrylate and norbornene groups) or through Michael addition chemistry with maleimides (MAL), vinylsulfones (VS), and acrylates (ACR). Michael-addition hydrogel networks form through a step- growth polymerization of the thiol and an electron-deficient group (e.g., VS), stemming from a two-part propagation process where a thiolate ion reacts with the VS group to form a carbon-based anion. The resulting anion reacts with another thiol group to form the next thiolate ion, leading to a repetitive process that generates a covalently crosslinked network[56].

In our studies, we chose to test poly(ethylene glycol) (PEG) hydrogels based on 4-arm PEG macromers with either terminal vinyl sulfone (PEG-4VS), acrylate (PEG-4ACR), or maleimide groups (PEG-4MAL) (Figure 2-1A). These polymers were chosen because they have the same PEG macromer backbone, similar molecular weight ≈20 000 Da, can be functionalized to pre- sent integrin-specific peptides that are cysteine-terminated via a similar Michael-type addition reaction,

and are crosslinked using di-thiolated crosslinkers at physiological pH and temperature under mild conditions[49], as opposed to UV crosslinking (Figure 2-1B). While all three chemical functionalities in PEG hydrogels have been studied for a wide range of mammalian cells (PEG-MAL[48,57,58], PEG-VS[59–61], PEG-ACR[62]), they have not been compared directly to each other for their impact on primary B cells for the induction of germinal centers. This is an important biomaterial consideration given the growing interest in building immune tissues[39,63,64], and the limited ability of natural matrices to control the microenvironment and integrin ligand presentation.

We first characterized the survival of our engineered stromal cell 40LB[6,38] (developed and provided by Daisuke Kitamura[4]), which are BALB/c 3T3 fibroblasts stably transduced with both T cell-derived CD40 ligand (CD40L) and FDC-secreted B cell activation factor. We tested conditions where the hydrogel macromers formed fast gels (<1 min) versus slow gels (>1 min) by tuning the pH of the PEG macromer and crosslinker type. Specifically, we tested the impact of the ratio of MMP-9 degradable crosslinker peptide (GCRDVPM↓SMRGGDRCG, referred to as VPM) with nondegradable crosslinker dithiothreitol (DTT). The rationale for using VPM was that our RNA sequencing has revealed a significantly higher expression of MMP-9 in germinal center B cells as compared to naïve B cells, but other MMPs were indifferent (Figure 2-1D). We observed high viability among fast gelling PEG-4MAL hydrogels irrespective of the crosslinker pH and VPM:DTT ratio (50 or 100% VPM) (Figure 2-1C). In contrast, PEG-4VS at 50% VPM or PEG-4MAL at either 50% or 100% VPM, both of which gelled slowly at lower PEG macromer (pH 6), showed cytotoxic effects on 40LB stromal cells (Figure 2-1C). There were no major differences between the stability of hydrogels (Figure 2-1D), except that slow gelling hydrogels formed a more uniform hydrogel than fast gelling ones, which can be attributed to wrinkling due to rapid pipetting

of fast gelling hydrogels. We, therefore, continued with formulations that showed high viability so that the effects can be delineated between B cells and 40LBs. We next examined the effect of polymer chemistry on B cell viability and induction of germinal center by co-encapsulating freshly isolated naïve murine B cells and 40LBs in the hydrogel organoid and culturing in the presence of 10 ng mL^{-1} IL-4, regular RPMI with 10% FBS and 1% antibiotics. In these initial studies, we chose a VCAM-1 mimicking peptide REDV, recently reported by us[7]. Interestingly, unlike 40LB cells, primary B cells failed to survive and proliferate in both vinyl sulfone and acrylate functionalized organoids (Figure 2-1E,F). Using CD19 as the surface biomarker of B cells and GL7 as surface epitope protein indicative of activated germinal center B cells, we found that B cells cocultured in PEG-4MAL organoids yielded a significantly higher number of $CD19^+$ B cells and germinal center-like ($CD19^+GL7^+$) B cells (Figure 2-1E-G). The GL7 expressing B cells (green) co-localized with 40LB stromal cells (yellow, spread), as revealed by confocal imaging studies (Figure 2-1H). Collectively, this is the first study, to the best of our knowledge, that establishes the superiority of advanced PEG-4MAL hydrogels with those functionalized with vinyl sulfone and acrylate, at least within the conditions tested, in regulating the fate of primary B cells toward induction of germinal centers.

To understand the molecular impact of the three hydrogels with similar underlying crosslinking mechanisms but different end-point functionalities, we examined the viability of B cells and generation of the apoptotic phenotype of germinal center- like B cells, i.e., $CD19^+GL7^+Fas^+$ cells. The number of viable B cells in PEG-4MAL organoids were significantly higher as determined using a live/dead flow cytometry assay (Figure 2-1I), in contrast to PEG-4VS and PEG-4ACR, alluding to the toxic effects of vinyl sulfone and acrylates. In addition, proliferative germinal center

B cells exhibit a phenotype that is characteristic of apoptosis-sensitive cells through increased levels of death- inducing molecule Fas[65]. Apoptosis through the expression of Fas is critical to the negative selection of germinal center B cells in vivo and for maintaining the efficacy of these specialized cells. We observed that the PEG-4MAL organoids generated a significantly higher number of $CD19^{+}GL7^{+}Fas^{+}$ B cells (Figure 2-1J), in contrast to PEG-4VS and PEG-4ACR organoids. The expression of Fas was, however, similar across all three polymer matrices, suggesting that the molecular impact of PEG-4MAL is through enhanced survival of primary B cells, in contrast to the toxicity induced by PEG-4VS and PEG-4ACR. Further temporal analysis of proliferative and apoptotic signals would be needed to understand the molecular impact of PEG-4-VS and PEG-4ACR on B cell signaling. It should be noted that the differences in the degree of macromer functionalization, the hydrolysis rate of the end group, and reactivity toward thiols could vary among the 3 macromers that are evaluated in the current study, and can impact final crosslink density and stiffness of the hydrogels[49], which may, in turn, affect B cell viability and germinal center induction. Further analysis of the impact of these factors on the proliferative and apoptotic signals is warranted.

2.4 Collagen 1 Mimicking Peptide Regulates Germinal Center Phenotype

Various follicle-associated stromal cells, including FDCs, express the collagen 1 gene. This is further supported by the presence of collagen conduits in B cell follicles and whole lymph node[66]. How collagen-mimicking matrices compare to fibronectin, vitronectin, or VCAM-1 ligands in inducing germinal centers remains unknown. Here, we examined three synthetic adhesive peptides with different integrin-binding specificities (Figure 2-2A). GFOGER is a triple- helical synthetic peptide derived from type I collagen with high binding affinity for $\alpha 1\beta 1$, $\alpha 2\beta 1$, $\alpha 10\beta 1$ and

$\alpha 11\beta 1$[67,68]. REDV is a tetrapeptide Arg-Glu-Asp-Val that mimics VCAM-1 in its ability to bind $\alpha 4\beta 1$ integrins[69] on B cells, and RGD is a short linear peptide present in vitronectin, fibronectin and other ECM proteins that bind several integrins, including $\alpha v\beta 3$, $\alpha v\beta 1$, and $\alpha 5\beta 1$[57,70,71]. We have previously shown that scrambled inactive peptides, such as GRDGSPC, do not engage integrins on B cells and fail to impact B cell receptors that are critical to downstream signaling and immune response[7], and therefore RDG only groups were not included in the current study. We did, however, incorporate RDG scramble peptides in the organoids as a filler to overcome solubility and viscosity issues when 100% GFOGER is used. Therefore, we used the 0.3 molar ratio of GFOGER, REDV, or RGD and 0.7 molar ratio of RDG. While all three peptides supported induction of nearly similar percentage of $CD19^+GL7^+$ germinal center phenotype cells by day 4 in presence of 40LB cells (Figure 2-2B), GFOGER peptide-functionalized PEG-4MAL organoids significantly increased the hallmark proliferative $CD19^+GL7^+Fas^+$ phenotype by ≈10% as compared to REDV and RGD peptides (Figure 2-2C). There were no significant differences between REDV and RGD peptides in the induction of $CD19^+GL7^+Fas^+$ population. Similarly, we observed a significant increase in the number of $CD19^+GL7^+Fas^+$ cells in GFOGER-organoids than in other matrices (Figure 2-2D). By day 6, the differences between matrices were lost, suggesting that matrices can play a role in the initial time course of induction of the germinal center phenotype (Figure 2-2E). Such studies are difficult to perform in vivo due to the migratory behavior of B cells that manifest unique cell cycle stages and emphasize the need for ex vivo immune organoids where nearly all cells are synchronized to similar states.

2.5 Materials and Methods

2.5.1 Biomaterials and Peptides

PEG-4MAL with 20 kDa molecular weight and ≥90% purity and PEG-4ACR with 21 kDa and >97% were purchased from Laysan Bio. PEG-4VS with 21 kDa molecular weight and >90% purity was purchased from Sigma. Integrin $\alpha v\beta 3$-binding RGD peptide (GRGDSPC, >90% purity), scrambled peptide (GRDGSPC, >90% purity), integrin $\alpha 4\beta 1$-binding REDV peptide (GREDVGC, >90% purity), GFOGER peptide (GYGGGPGPPGPPGPPGPPGPPGFOGERGPPGPPGPP GPPGPPGPC, ≥90% purity), and matrix metalloproteinase (MMP)-9 degradable VPM peptide (GCRDVPMSMRGGDRCG, >90% purity) were purchased from Aapptec. Nondegradable dithiothreitol (DTT) crosslinker was purchased from Sigma Aldrich. All components were reconstituted in 0.01 m HEPES buffer with pH 7.4.

2.5.2 Stromal Cell Culture and Mitomycin-c Treatment

40LB stromal cells, genetically modified from NIH/3T3 fibroblasts to express CD40 ligand and produce B cell activating factor, as described previously[4,6,7,37,38,72], were obtained from Dr. Daisuke Kitamura[4]. 40LB cells were cultured in Dulbecco's Modified Eagle Medium containing 10% fetal bovine serum and 1% penicillin-streptomycin (P/S) and routinely passaged at 90% confluency. Before encapsulation in organoids, 40LB were mitotically inhibited via incubation with 0.01 mg mL^{-1} mitomycin-C at 37 °C for 45 min.

2.5.3 Naïve B Cell Isolation from Mice

For experiments involving wildtype (WT) B cells, spleens were harvested from female C57BL/6 mice, aged 8–15 weeks, from the Jackson Laboratory. Where indicated, mice aged >2 years were

used to compare the effects of aging. Spleens were dissociated using a sterile plunger, as previously described[38], and the cell suspension was incubated in RBC lysis buffer for 5 min at room temperature to remove red blood cells. Naïve B cells were purified from the splenocyte suspension by negative isolation using an EasySep Mouse B Cell Isolation Kit from Stem Cell Technologies, according to the manufacturer's instructions. All animals were handled in compliance with the procedures approved by the Institutional Animal Care and Use Committee (IACUC) at Cornell University and the University of California, San Francisco.

2.5.4 Organoid Fabrication

Synthetic immune organoids containing 7.5% w/v of PEG-4MAL or PEG-4VS or PEG-4ACR were fabricated using the corresponding PEG macromer, adhesives peptides, and crosslinkers. PEG-4MAL was functionalized at pH 7.4 with thiolated adhesive peptides RGD, REDV, or GFOGER at a 4:0.3 MAL-to-peptide molar ratio, and RDG scramble at a 4:0.7 MAL-to-peptide molar ratio for 30 min at 37 °C. MMP9-degradable VPM peptide and nondegradable DTT crosslinkers were combined at a 1:1 VPM-to-DTT molar ratio and a 4:1.5 MAL-to-crosslinker molar ratio and adjusted to pH 5–6. 40 000 Naïve B cells and 40 000 40LB stromal cells were suspended in the crosslinker solution, and 5 µL of crosslinker-cell suspension was injected into 5 µL functionalized PEG-MAL in each well of a nontreated 96 well plate. The droplet was mixed rapidly via pipet and cured at 37 °C for 15 min. Post-incubation, Roswell Park Memorial Institute (RPMI) 1640 media containing 10% FBS, 1% P/S, and 10 ng mL^{-1} interleukin-4 (IL-4, Peprotech) was added to each organoid. The media was replenished every 3 days.

2.5.5 Flow Cytometry

On days 4 or 6, organoids were rinsed in 1X PBS and enzymatically digested in 125 U mL^{-1} collagenase type 1 (Worthington Biochemical) for 1 h at 37 °C. Enzyme activity was terminated by the addition of buffer containing serum, and the cells were filtered to remove organoid debris using 96 well MultiScreen Mesh Filter Plates (EMD Millipore). Cells were resuspended in 1X PBS with viability dye (Thermo Fisher) and incubated in the dark on ice for 30 min. Cells were then resuspended in FACS Buffer (PBS^{++} with 2% FBS, 1% P/S, and 0.005×10^{-3} M EDTA) containing antibodies against cell surface antigens and incubated in the dark on ice for 1 h. Post-incubation, the cells were washed and resuspended in FACS Buffer. For intracellular antigens, the cells were fixed for 30 min in Fixation/ Permeabilization Buffer (eBioscience Foxp3/Transcription Factor Staining Buffer) and incubated in permeabilization buffer containing antibodies for 1 h on ice, protected from light. Anti-mouse monoclonal antibodies targeting cell surface antigens included anti-GL7 (FITC, PE, eFluor660; clone GL 7; Thermo Fisher), anti-B220 (PE-Cy7; clone RA3-6B2; Thermo Fisher), anti-Fas (APC; clone 15A7; Thermo Fisher), anti-CD19 (FITC; clone 1D3; Thermo Fisher), anti-CD138 (FITC; clone 300506; Thermo Fisher), anti-IgD (PE; clone 11–26C; Thermo Fisher), and anti-CD38 (APC; clone 90; Thermo Fisher). Anti-mouse monoclonal antibodies targeting intracellular antigens included anti-H3k27me3 (AF488, AF647; clone C36B11; Cell Signaling), anti-EZH2 (eFluor 660; clone AC22; Thermo Fisher), anti-CBP (FITC, AF488; clone C-1; Santa Cruz), anti-H3k27ac (AF647; clone D5E4; Cell Signaling), anti-IRF4 (FITC, PE, PE-Cy7; clone 3E4; Thermo Fisher), and anti-BCL6 (PE, APC; clone BCL-DWN; Thermo Fisher).

2.5.6 Imaging Analysis

For imaging, organoids were cultured in glass-bottom 35 mm dishes or 96-well glass bottom dishes. After 4 days in culture, organoids were fixed in 4% paraformaldehyde in PBS for 15 min, permeabilized with 0.5% Triton-X-100 in PBS for 30 min, and blocked with normal 20% normal goat serum for 30 min. Organoids were then incubated with fluorescence-conjugated primary antibodies (anti-GL7-AF488, Thermo Fisher, 1:200 dilution; anti-NP-AF647, Novus Biologicals, 1:200 dilution; rat anti-IgM) overnight. After washing with PBS, organoids were incubated with secondary antibodies (goat anti-rat IgG, AFP647, Thermo Fisher) and actin stain (phalloidin-AF568, Thermo Fisher; phalloidin-AF555, Thermo Fisher) and nuclear stain (DAPI) for 4 hours. Organoids were washed and resuspended in PBS. The organoids were imaged on a Zeiss LSM710 confocal microscopes. Bright field images were taken on an EVOS XL Core microscope.

2.5.7 Statistical Analysis

Statistical analysis was performed using GraphPad Prism software. Data analysis used an unpaired two-tailed t-test or one-way analysis of variance (ANOVA) with Tukey's post hoc test or two-way ANOVA with Sidak's multiple comparison test. Quantitative analyses as scatter or bar graphs are presented as means ± SEM. In all studies, *$P < 0.05$, **$P < 0.01$, and ***$P < 0.001$ unless otherwise stated. Nonsignificance is denoted by "ns."

2.6 Acknowledgements

The authors acknowledge financial support from the National Institute of Allergy and Infectious Diseases of the US National Institutes of Health (5R01AI132738-03 awarded to A.S.), and in part by the US National Science Foundation CAREER award (DMR-1554275 awarded to A.S.) and

the Innovative Molecular Analysis Technology program of the US National Cancer Institute (NIH R33-CA212968-01 awarded to A.S.). The authors acknowledge financial support from the Immunoengineering T32 training grant to S.P. (NIH and NIBIB, 1T32EB023860-01A1) and NIH 1S10RR025502 funding for the shared Zeiss LSM 710 Confocal Microscope, awarded to the Cornell University Biotechnology Resource Center. Opinions, interpretations, conclusions, and recommendations are those of the authors and are not necessarily endorsed by the funding agency.

2.7 Figures

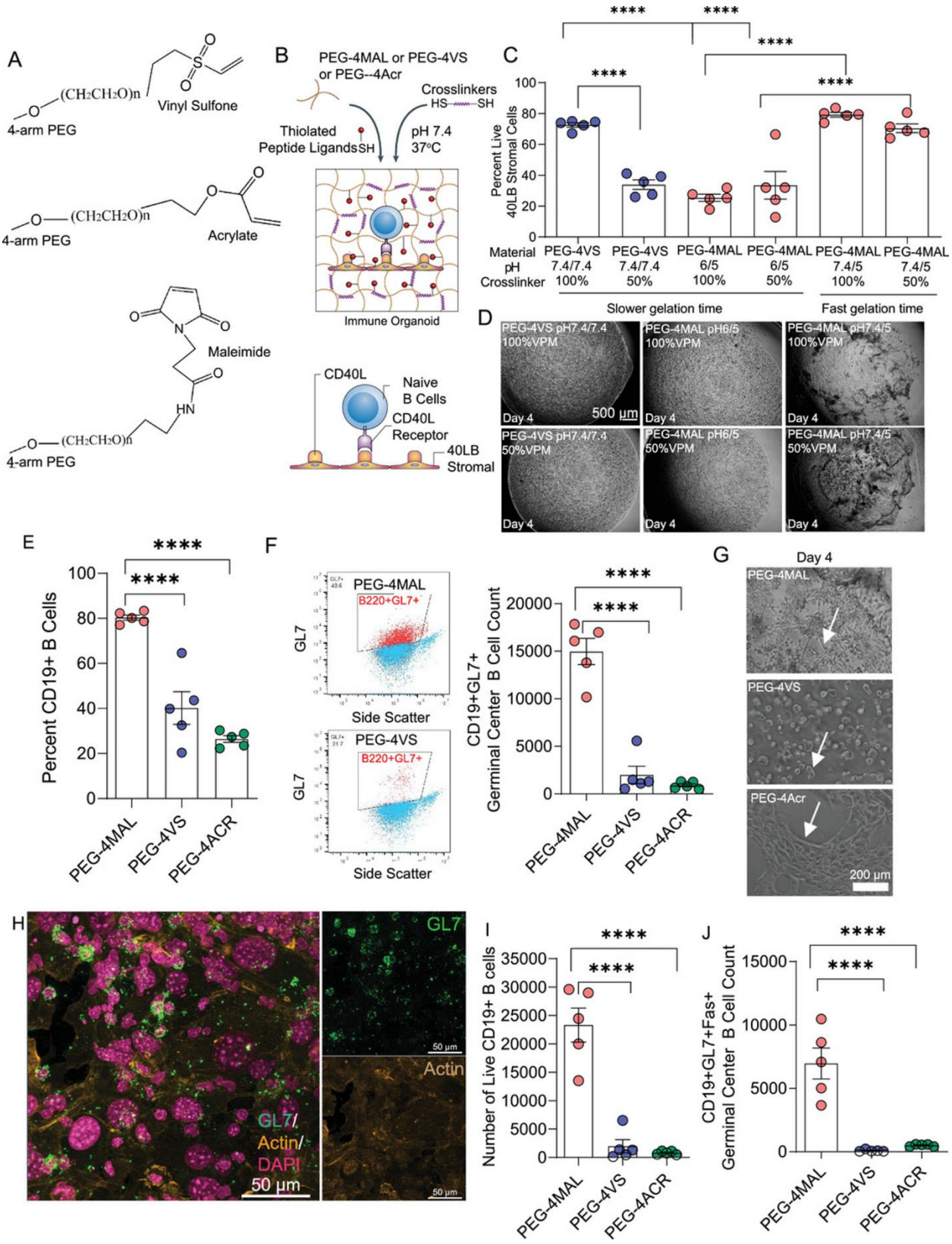
A
(CH2CH2O)n
Vinyl Sulfone
4-arm PEG
(CH2CH2O)n
Acrylate
4-arm PEG
Maleimide
HN
(CH2CH2O)n
4-arm PEG
B
PEG-4MAL or PEG-4VS
or PEG--4Acr
Crosslinkers
HS SH
Thiolated
Peptide Ligands SH
pH 7.4
37°C
Immune Organoid
CD40L
Naive
B Cells
CD40L
Receptor
40LB
Stromal
C
****
****
****
****
****
Percent Live
40LB Stromal Cells
100
80
60
40
20
0
Material PEG-4VS PEG-4VS PEG-4MAL PEG-4MAL PEG-4MAL PEG-4MAL
pH 7.4/7.4 7.4/7.4 6/5 6/5 7.4/5 7.4/5
Crosslinker 100% 50% 100% 50% 100% 50%
Slower gelation time
Fast gelation time
D
PEG-4VS pH7.4/7.4
100%VPM
PEG-4MAL pH6/5
100%VPM
PEG-4MAL pH7.4/5
100%VPM
Day 4
500 µm
PEG-4VS pH7.4/7.4
50%VPM
PEG-4MAL pH6/5
50%VPM
PEG-4MAL pH7.4/5
50%VPM
E
****
****
Percent CD19+ B Cells
100
80
60
40
20
0
PEG-4MAL
PEG-4VS
PEG-4ACR
F
PEG-4MAL
B220+GL7+
GL7
Side Scatter
PEG-4VS
B220+GL7+
GL7
Side Scatter
****
****
CD19+GL7+
Germinal Center B Cell Count
20000
15000
10000
5000
0
PEG-4MAL
PEG-4VS
PEG-4ACR
G
Day 4
PEG-4MAL
PEG-4VS
PEG-4Acr
200 µm
H
GL7/
Actin/
DAPI
50 µm
GL7
50 µm
Actin
50 µm
I
****
****
Number of Live CD19+ B cells
35000
30000
25000
20000
15000
10000
5000
0
PEG-4MAL
PEG-4VS
PEG-4ACR
J
****
****
CD19+GL7+Fas+
Germinal Center B Cell Count
15000
10000
5000
0
PEG-4MAL
PEG-4VS
PEG-4ACR

Figure 2-1: Hydrogel macromer end-modification chemistry regulates the survival and differentiation of primary immune cells.

A) Chemical structure of the vinyl sulfone, acrylate, and maleimide functional groups at the end of four-arm PEG.

B) Schematic of immune organoid formation with co-cultured CD40L- and BAFF-presenting stromal cells and primary, naive B cells.

C) Effects of pH and degradability on 40LB cell viability in PEG-4VS and PEG- 4MAL hydrogels.

D) Representative brightfield images illustrating the effects of pH and degradability on stromal cell network formation in PEG-4VS and PEG-4MAL organoids.

E) Quantitative flow cytometric analysis of CD19+ B cell in four-arm PEG hydrogels modified with maleimide, vinyl sulfone, or acrylate, indicating survival in hydrogels.

F) Flow cytometric gating strategy and germinal center-like B cell (CD19+GL7) formation in four-arm PEG hydrogels modified with maleimide, vinyl sulfone, and acrylate.

G) Effects of maleimide, vinyl sulfone, and acrylate functionalization on stromal cell network formation and survival of B cells in PEG-based organoids.

H) Confocal imaging of germinal center-like B cell (GL7+) and its relative localization with 40LB stromal in PEG-4MAL organoids. Green: GL7, Yellow: Actin (false color from red), Magenta: DAPI (false color from blue).

I) Effect of four-arm PEG end-modification chemistry on cell viability of CD19+ B cells cultured in organoids for 4 days.

J) Quantitative flow cytometric analysis of CD19+GL7+Fas+ germinal center-like B cell formation after 4 days of culture in four-arm PEG hydrogels modified with maleimide, vinyl sulfone, or acrylate. All data represent mean ± S.E.M. and were analyzed via one-way ANOVA

with Tukey's posthoc multiple comparisons test. ****p < 0.0001, ns = not significant; N = 5.

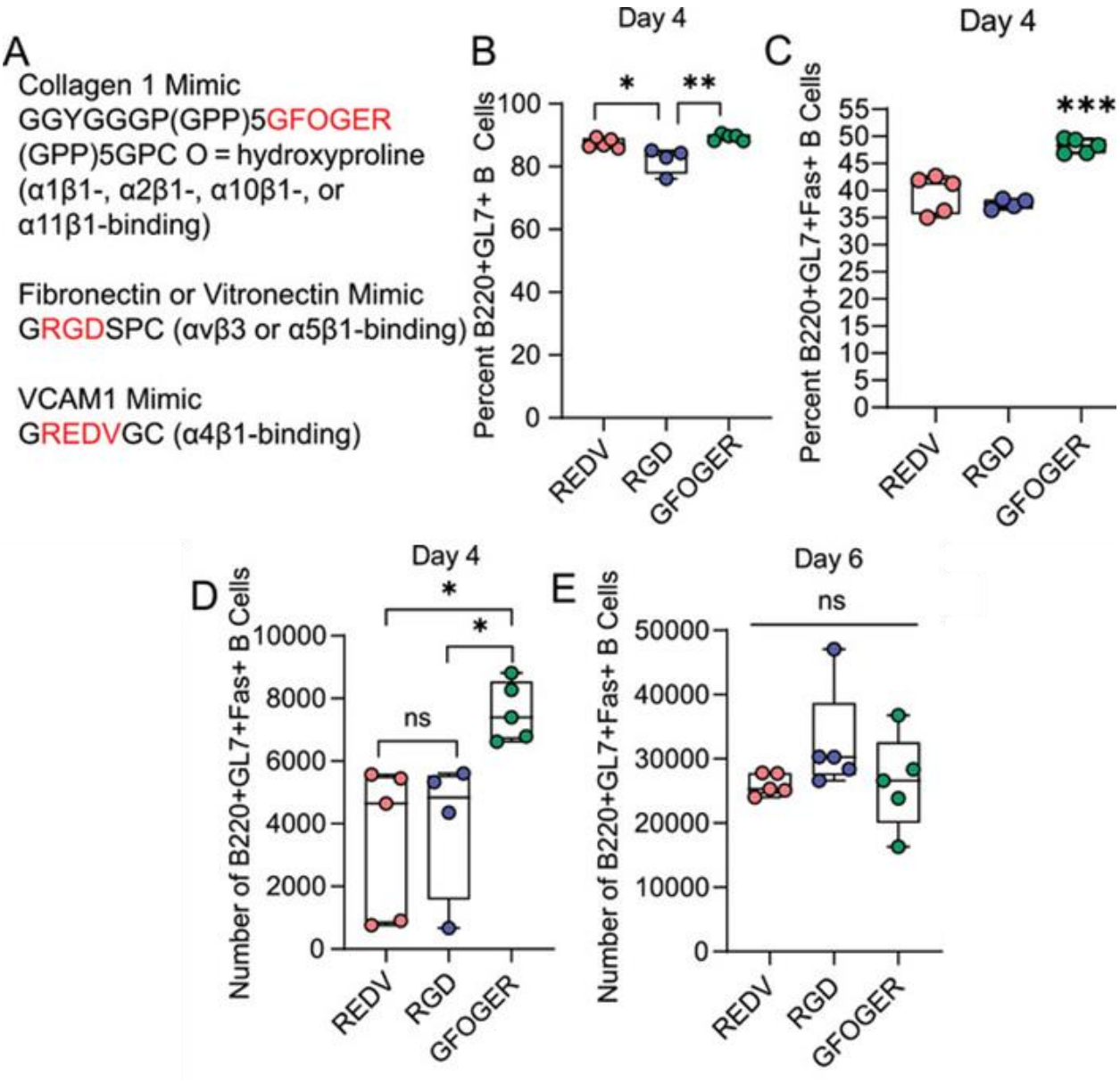

Figure 2-2: Collagen-mimicking GFOGER peptide ligand differentially regulates germinal center-like B cell activation and signaling.

A) Sequences of integrin-binding peptides incorporated into PEG-4MAL organoids.

B,C) Effects of GFOGER peptide ligand on the percent of B) $B220^{+}GL7^{+}$ B cells and

C) proliferative $B220^{+}GL7^{+}Fas^{+}$ B cells, in contrast to VCAM-1-like and RGD peptide ligands in

organoid grown cultures of naïve B cells with 40LB and IL-4.

D,E) Time-dependent effects of varying integrin ligand on the number of $B220^{+}GL7^{+}Fas^{+}$ cells on D) Day 4 and E) Day 6. All data represent mean ± S.E.M. and were analyzed via one-way ANOVA with Tukey's posthoc multiple comparisons test. *$p<0.05$, **$p<0.01$, ***$p < 0.001$, ns = not significant; N = 5.

CHAPTER 3

Lymphoid tumor microenvironment controls BCR signaling in lymphomas

3.1 Abstract

Activated B cell-like diffuse large cell lymphoma (ABC-DLBCL) develop in B cell follicles of secondary lymphoid organs and are among the most drug-resistant DLBCLs. ABC-DLBCLs are characterized by constitutive activation of NF-κB, driven by activation of the B cell receptor (BCR), toll-like receptor (TLR), and PI3K pathways due to activating mutations within the BCR-TLR-PI3K superpathway. However, these activating mutations are insufficient to explain the limited response to BCR pathway targeted therapies. Here, we demonstrate that cellular and biophysical factors in the lymphoid tumor microenvironment (Ly-TME) modulate the cooperative signaling in ABC-DLBCLs. We identified microenvironment components that mediated resistance to standalone MALT1 inhibitors and determined their effect on the BCR-PI3K-TLR superpathway. Our studies define the complex crosstalk between malignant ABC-DLBCL cells and selective components of Ly-TME to uncover previously unexplored resistance to clinical inhibitors of the BCR pathway.

3.2 Introduction

Increased understanding of the molecular mechanisms underlying non-Hodgkin's lymphoma (NHL) has opened the door for targeted therapy in aggressive diffuse large B-cell lymphoma (DLBCL). Based on distinct gene expression profiles, DLBCLs are classified into B cell receptor signaling-driven activated B cell-like (ABC) subtypes and epigenetics-driven germinal center B cell-like (GCB) subtypes[73,74], but have widely divergent outcomes[75]. ABC-DLBCL is the most chemo-resistant subtype to the frontline therapy R-CHOP, with 40% of patients experiencing no

response or relapse[76,77]. Genetic alterations interact with clinical factors to impact overall survival in DLBCL[73,74,78–80]. Improved therapies are needed for all DLBCLs, but most urgently for the activated B cell-like (ABC) DLBCL subtypes with distinct gene expression profiles and immune microenvironments, including the presence of CD4+ T cells[81].

The survival of ABC-DLBCLs depends on the constitutive activation of NF-κB through the B cell receptor (BCR), toll-like receptor (TLR), and phosphoinositide-3-kinase (PI3K) pathways[73,82]. Several inhibitors targeting these pathways are therefore being explored[81,83]. Ibrutinib, an irreversible inhibitor of Bruton's tyrosine kinase (BTK), displayed activity in clinical trials for ABC-DLBCL patients with CD79 mutations but only produced responses in 37% of total ABC-DLBCL cases partially due to downstream mutations, such as CARD11[76]. The mechanisms through which ABC-DLBCLs are resistant to current therapies are not fully understood. These BCR and TLR pathways are activated in part due to hallmark ABC-DLBCL mutations (i.e., CD79A/B, myeloid differentiation primary response 88 (MYD88), caspase recruitment domain-containing protein 11 (CARD11), and more). However, the chronic signaling through mutations is relatively weak. We hypothesize that complex growth signals from lymph node tumor microenvironment (Ly-TME) further stimulate BCR and TLR pathways in ABC-DLBCLs, causing resistance to therapeutics.

The CBM complex, which includes CARD11, B-cell lymphoma/leukemia 10 (BCL10), and mucosa-associated lymphoid tissue lymphoma translocation protein 1 (MALT1), integrates signals from the cooperative BCR, TLR, and PI3K pathways to activate NF-κB and presents a downstream target that can disrupt many of the upstream mutations that drive aberrant signaling. MALT1

protein is necessary for ABC-DLBCL proliferation and survival by leading to constitutive NF-κB signaling through its function as a scaffold protein in IκB kinase (IKK) complex activation[84] and as a paracaspase that cleaves inhibitors of NF-κB[82,85,86]. As the only paracaspase in the human genome, MALT1 also has a structurally unique enzymatic pocket, offering the possibility of developing targeted inhibitors with high specificity. Hence, targeting MALT1 can potentially impact a broad cross-section of ABC-DLBCL patients with reduced off-target effects and without causing toxicity to other organs[82,86,87]. Irreversible MALT1 catalytic pocket inhibitors, MI-2 14, and an irreversible MALT1-selective, peptidomimetic inhibitor, Compound 3 (C3)[87] display activity against ABC-DLBCLs in vitro and in vivo. Similar results have been reported for compounds that inhibit MALT1 through an allosteric, reversible mechanism[88]. Although MALT1 inhibition has emerged as a promising therapeutic approach against ABC-DLBCLs, tumors can engage feedback mechanisms that limit the activity of signaling pathway inhibitors, as has indeed been shown for MALT1 inhibitors as well[82]. Even though we understand that the Ly-TME is composed of immune cells, stromal cells, and extracellular matrix (ECM)[89], to date, we do not fully understand the impact of Ly-TME on the CBM complex and their cooperation with constitutively active pathways in ABC-DLBCLs, and consequently, on the efficacy of inhibitors and/or agonists to adequately suppress these networks. Constitutive BCR engagement by cognate self-antigen drives BCR clustering in ABC-DLBCL[90].

We identify PEG-based polymers that support lymphoma growth. We identify TME components that induce MALT1 and TLR signaling and induce a high degree of coordination of the BCR-PI3K-TLR superpathway to mediate resistance to standalone MALT1 inhibitors. We identify TME components that upregulate BCR clustering.

3.3 End Group of Hydrogel and Lymphoma Organoids

Lymphomas have not been characterized together in maleimide, vinylsulfone, and acrylate end group hydrogels. We used Michael-addition chemistry to crosslink gels with MMP-9 degradable crosslinker VPM and nondegradable crosslinker DTT. To first test lymphoma growth in various polymer end group hydrogels, we used a murine B cell lymphoma cell line, WEHI-231 to determine lymphoma viability. Lymphoma cells in PEG-MAL organoids proliferated and formed clusters, but PEG-VS and PEG-ACR organoids had disperse lymphoma cells after 4 days (Figure 3-1A). As with primary B cells in Section 2.3, WEHI-231 grew in PEG-4MAL hydrogels but showed poor survival in PEG-4VS and PEG-4ACR (Figure 3-1B,C). The longer gelation time and therefore longer exposure to uncrosslinked VS and ACR groups could have a cytotoxic effect on lymphoma cells. The remaining lymphoma organoid studies used PEG-4MAL hydrogels.

3.4 Lymphoma Susceptibility to Drug, Stromal Support, and Tumor Microenvironment

Inside the hydrogels, spherical $CD20^+$ DLBCLs localized over the spread CD40L-presenting stromal cells within 48 hr (Figure 3-2). The CD40L presentation resulted in a significantly reduced cell death of CD20+ ABC-DLBCL cells (11-16%) in response to another 48 hr treatment with MALT1 inhibitor (MI-2), added to the cell culture media in which the PEG-4MAL hydrogel-based organoids were growing (Figure 3-3A). Both 125 nM and 2000 nM MI-2 doses effectively killed 84-99% of $CD20^+$ ABC-DLBCL cells in organoid conditions that did not present CD40L compared to those that presented CD40L (Figure 3-3). CD40L presentation further attenuated the effect of MALT1 inhibitor on cell proliferation, as shown by a dye dilution assay (Figure 3-3B). These results suggest that CD40L-mediated signaling from T cells can affect the efficacy of MALT1 inhibitor and the resistance is more prevalent in 3D physiological conditions than in 2D.

We next sought to understand whether the collagen-mimicking GFOGER peptide, which binds to multiple β1 integrin dimers, would induce similar changes in MALT1 inhibition and signaling. The GFOGER peptide adopts a triple-helical conformation that mimics collagen I and is necessary for its bioactivity, including binding to integrins[91]. HBL1 cells cultured in GFOGER-organoids had an LC50 of 178.5 nM, approximately two-fold higher than that in RGD and almost four-fold than that in REDV (Figure 3-4A). MALT1 in GFOGER-organoids was higher than REDV-organoids (Figure 3-4B).

We next determined whether IL10, which is highly expressed in ABC-DLBCL patients and supports ABC-DLBCL survival and proliferation[87,92], was dependent on integrin-binding ligands. MALT1 controls cytokine expression, including IL10, by cleaving mRNA decay regulators, such as roquin-1, an E3 ubiquitin ligase that is a master regulator of the immune system homeostasis[87]. We have previously reported that MALT1 inhibition downregulates IL10[87] and in the current study, we observed that MI-2 LD50 values and IL10 secretion values had the same ascending order (REDV < RGD < GFOGER), illustrating how TME-mediated IL10 secretion can affect MALT1 inhibitor efficacy. (Figure 3-4C). Overall, these results highlight that cross-talks between the ECM and integrins on ABC-DLBCL cells can modulate MALT1 signaling and the efficacy of MALT1 inhibitor. Notably, CD40L inclusion overcame the ECMs effect and led to a significant resistance to MALT1 inhibitor regardless of peptide presentations (Figure 3-4D).

3.5 BCR Clustering in Lymphoma Organoids

Malignant B cells co-opt multiple proliferative and survival pathways activated downstream of the

BCR to promote their growth, survival, and response to therapeutics[83]. We hypothesized that the binding of CD40L to CD40 might intersect with BCR pathway signals, upregulating the expression of BTK, MALT1, BCL10, and NF-κB. To investigate how CD40L stromal signals and peptide ligand affects BCR clustering, we imaged single DLBCL cells within organoids and counted IgM BCR puncta per cell (Figure 3-5A,B). Addition of CD40L increased the number of IgM BCR puncta in both HBL1 and OCI-Ly10, suggesting that stromal CD40L boosts BCR engagement (Figure 3-5C,D). DLBCLS in GFOGER-organoids had more IgM BCR puncta than DLBCLs in REDV-organoids, suggesting that GFOGER induced increase in BCR clustering leads to enhanced BCR pathway signaling.

3.6 BCR Signaling in Lymphoma Organoids

We next determined whether CD40L presentation increased downstream pBTK expression, as indicated by phosphorylation of its Tyr551 residue (Figure 3-6A). Subsequent treatment of BTK inhibitor Ibrutinib paralleled the trends observed after MALT1 inhibition (Figure 3-6B), supporting that CD40L reduced cell death. The inclusion of CD40L increased MALT1 and pNF-κB expression in human PDX cells (Figure 3-6C,D), supporting the hypothesis that CD40L enhances BCR pathway signaling, which contributes to MALT1 inhibitor resistance in ABC-DLBCLs.

3.7 Materials and Methods

3.7.1 Polymer and Peptides

Four-arm maleimide-functionalized polyethylene glycol (PEG-4MAL) with 20 kDa molecular weight and ≥ 90% purity was purchased from Laysan Bio, Inc. Peptides (>95% purity) were

purchased from AAPPTec and included collagen 1 mimic "GFOGER" (GGYGGGP(GPP)$_5$**GFOGER**(GPP)$_5$GPC, where O=hydroxyproline), fibronectin/vitronectin mimic "RGD" (G**RGD**SPC), VCAM1 mimic "REDV" (G**REDV**GC), control peptide (G**RDG**SPC), and protease-sensitive crosslinker (GCRD**VPMS**↓MRGGDRCG). Nondegradable crosslinker dithiothreitol (DTT) was purchased from Sigma Aldrich. All components were reconstituted in 0.01 M HEPES with pH 7.4.

3.7.2 Chemical Compounds

Mitomycin C was purchased from Santa Cruz Biotechnology. Idelalisib, dasatinib, masitinib, and ibrutinib were purchased from Selleckchem. MALT1 inhibitor, MI-2, was purchased from Tocris Bioscience, and Compound 3 (C3) was obtained from Ari Melnick (Weill Cornell Medicine, New York, NY). Previously listed chemicals were reconstituted in DMSO. CpG ODN 2395 was purchased from InvivoGen and reconstituted in endotoxin-free water.

3.7.3 Cell Culture

OCI-Ly3, OCI-Ly10, and HBL1 were obtained from Ari Melnick (Weill Cornell Medicine, New York, NY). OCI-Ly3 and OCI-Ly10 were cultured in Iscove's medium supplemented with 20% FBS, and HBL1 was cultured in Roswell Park Memorial Institute (RPMI) 1640 medium supplemented with 10% FBS and 10 mM HEPES. All ABC-DLBCL cells were grown in the presence of penicillin G/streptomycin and 2 mM L-Glutamine. CD40L-L cells, genetically modified L cells to express human CD40 ligand, as described previously were obtained from Dr. Hideki Ueno and cultured in RPMI supplemented with 10% FBS and 80 μg/ml geneticin (Thermo Fisher). WEHI-231 was obtained from Jason Cyster (UCSF, San Francisco, CA) and cultured in

RPMI with 10% FBS, 1% P/S, 10 mM HEPES, Glutamax, and 2-mercaptethanol. All cells were grown at 37˚C in a humidified atmosphere of 5% CO2.

3.7.4 Hydrogel-based Organoid fabrication

Organoids were formed in synthetic hydrogels made of PEG-4MAL with typically a 7.5% (w/v) macromer concentration. PEG-4MAL was first functionalized at pH 7.4 with thiolated adhesive peptides RGD, REDV, GFOGER or control peptide RDG for 30 minutes at 37˚C. While RGD, REDV were used at 3 mM concentration, due to size constraints, GFOGER was functionalized at lower molarity (1 mM), with all additional maleimide sites occupied by the scrambled control peptide to make up for 3 mM total peptide concentration. This decrease in molarity did not significantly alter the MI-2 LD50 of HBL1 cells in RGD- or REDV-organoids. Protease-sensitive crosslinker (VPM) and non-degradable crosslinker (DTT) were combined at a 1:1 molar ratio and adjusted to pH 6. Briefly, before combining the polymer and crosslinker, cell mixtures were suspended in the crosslinker solution. When using cell lines, cell mixtures included 40,000 cells ABC-DLBCL cells with or without 40,000 CD40L-L cells. For PDX samples, mixtures included 80,000-200,000 PDX cells with or without 50,000 CD40L-L cells. After mixing, cell-crosslinker solutions were immediately injected into an equal amount of functionalized PEG-4MAL located in a well of a nontreated 96 well plate. The ensuing droplet was mixed via pipetting and cured for 15 minutes at 37˚C. Appropriate media was added post-incubation to begin organoid cultures. The media was replenished every two days. In some experiments, organoid stiffness was modulated by varying PEG-4MAL w/v or the ratio of adhesive peptide to crosslinker.

3.7.5 Flow Cytometry

At the end of the desired culture time, organoids were washed with PBS and enzymatically digested in 125 U/ml type I collagenase (Worthington Biochemical) for 1 hour at 37˚C. Buffer containing serum was added at the end of this incubation to terminate the enzymatic activity. Organoid debris was removed using 96 well MultiScreen Mesh Filter Plates (EMD Millipore), and the ensuing cells were resuspended in FACS Buffer (PBS++ with 2% FBS, 1% penicillin G/streptomycin, and 5 mM EDTA). Cells were first stained with antibodies against cell surface antigens and incubated in the dark on ice for 1 hour. For intracellular antigens, cells were then fixed and permeabilized using the eBioscienceTM Foxp3/Transcription Factor staining buffer (Thermo Fisher) set or BD PhosflowTM fix buffer I when antigen phosphorylation was of interest. After fixation, cells were incubated in permeabilization buffer with antibodies against intracellular antigens for 1 hour on ice. Cells were analyzed using an Accuri C6 flow cytometer. Data were analyzed using FlowJo to determine the percentage or number of positive cells, median and mean fluorescent intensities, and the distribution of fluorescent intensity.

Human antibodies included anti-BCL10 (AF488; clone EP606Y; abcam), anti-CD20 (FITC, PE, PE-Cy7, APC; clone 2H7; Thermo Fisher), anti-MALT1 (AF647; clone EP603Y; abcam), anti-phospho-BTK (PE; clone M4G3LN; Thermo Fisher), phospho-NFκB p65 (PerCP-eFluor 710; clone B33B4WP; Thermo Fisher), phospho-S6 (Ser235/236) (AF647; clone D57.2.E; Cell Signaling Technology), phosphor-SRC (Tyr418) (PE; SC1T2M3; Thermo Fisher), and TLR9 (FITC, PE, APC; eB72-1665; Thermo Fisher). Canine antibodies included anti-CD3, anti-CD4, anti-CD20 (clone 6C12; InvivoGen), anti-CD45, anti-MHC II, and anti-Thy-1. Additional stains included CellTraceTM CFSE (Thermo Fisher) to measure cell proliferation as well as

LIVE/DEADTM fixable stains (Green Dead Cell, Far Red Dead Cell; Thermo Fisher) or propidium iodide (Thermo Fisher) to measure cell viability.

3.7.6 Organoid Treatment

Organoids were fabricated, and cells were allowed to interact with the surrounding environment for 48 hours prior to treatment with any inhibitors. MI-2, was then added for 48 hours. After the desired treatment time, organoids were then degraded as previously described. Cells were subsequently stained with CD20 and LIVE/DEADTM fixable stains and analyzed via flow cytometry. Live $CD20^{+}$ cell numbers were normalized to vehicle-treated organoids, and GI50 values were calculated using GraphPad Prism 8 software. To visualize live and dead cells in organoids, separate organoid samples that had undergone the desired treatment regimen were washed with $PBS^{-/-}$ and stained in 4 nM Calcein AM and 4 nM Ethidium Homodimer in media for 45 minutes at 37˚C. The staining solution was then replaced with fresh media, and organoids were directly imaged for live (green) and dead (red) populations on a Nikon TE200U microscope.

3.7.7 Imaging Analysis

On day 4, organoids were fixed in 4% paraformaldehyde for 15 minutes at room temperature and rinsed with PBS twice. Cells were permeabilized with 0.5% Triton-X 100 for 30 minutes and washed with PBS. Organoids were resuspended in 20% normal donkey serum blocking buffer. Primary antibody staining solution (rabbit anti-human CD20, Thermo Fisher; mouse anti-human IgM, Thermo Fisher) was added and incubated overnight at 4°C. After incubation in primary staining solution, organoids were washed with PBS and incubated in secondary staining solution (donkey anti-rabbit IgG AFP488, Thermo Fisher; donkey anti-mouse IgG AFP647, Thermo

Fisher; DAPI; phalloidin AF555, Thermo Fisher) for 4 hours at 4°C. Organoids were rinsed with PBS twice and imaged on Zeiss LSM700 and Zeiss LSM710 confocal microscopes. IgM puncta were counted manually on maximum intensity projections of single-cell zstack images. Numbers of puncta were plotted on GraphPad Prism.

3.8 Acknowledgements

The authors acknowledge financial support from the US National Cancer Institute (1R01CA238745-01A1 awarded to A.S.), the Innovative Molecular Analysis Technology program of the US National Cancer Institute (NIH R33-CA212968-03 awarded to A.S.), and the US Department of Defense (Grant number: W81XWH-17-1-0215, awarded to A.S.). The authors also acknowledge academic scholarship support from the Immunoengineering T32 Training grant to S.B.S. (NIH and NIBIB, IT32EB023860-01A1).

3.9 Figures

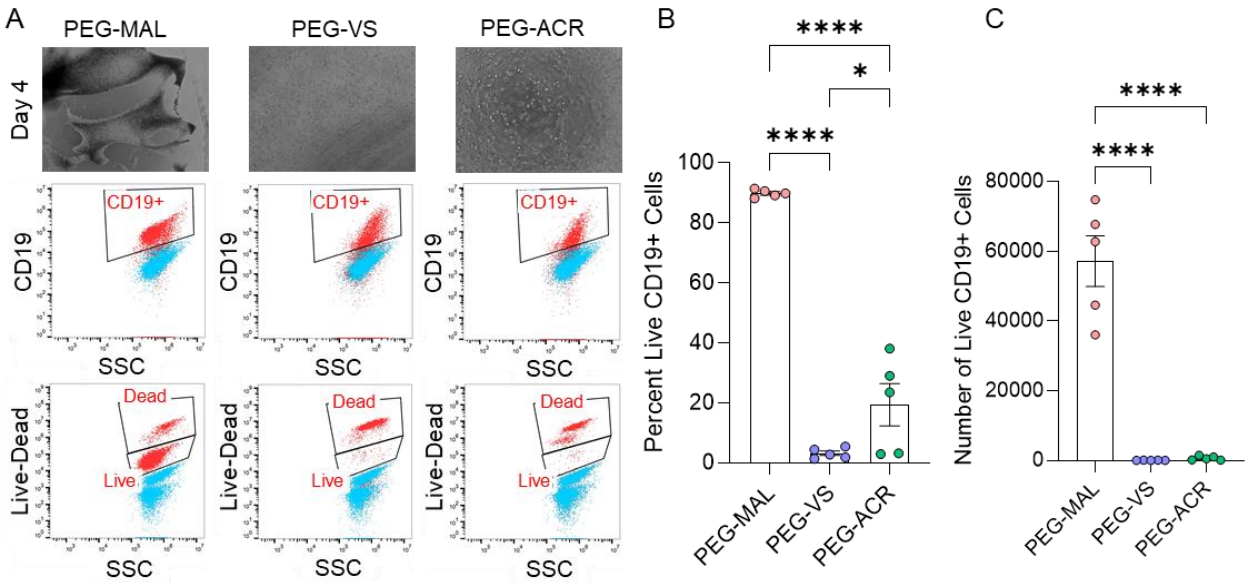

Figure 3-1: Hydrogel macromer end-modification chemistry regulates the survival of murine

lymphoma cells.

A) Bright field images of organoids and representative flow cytometry gating for CD19 and Live-Dead staining.

B-C) WEHI-231 viability in PEG-MAL, PEG-VS, and PEG-ACR. 1-way ANOVA test *P<0.05, ****P<0.0001 (n = 5).

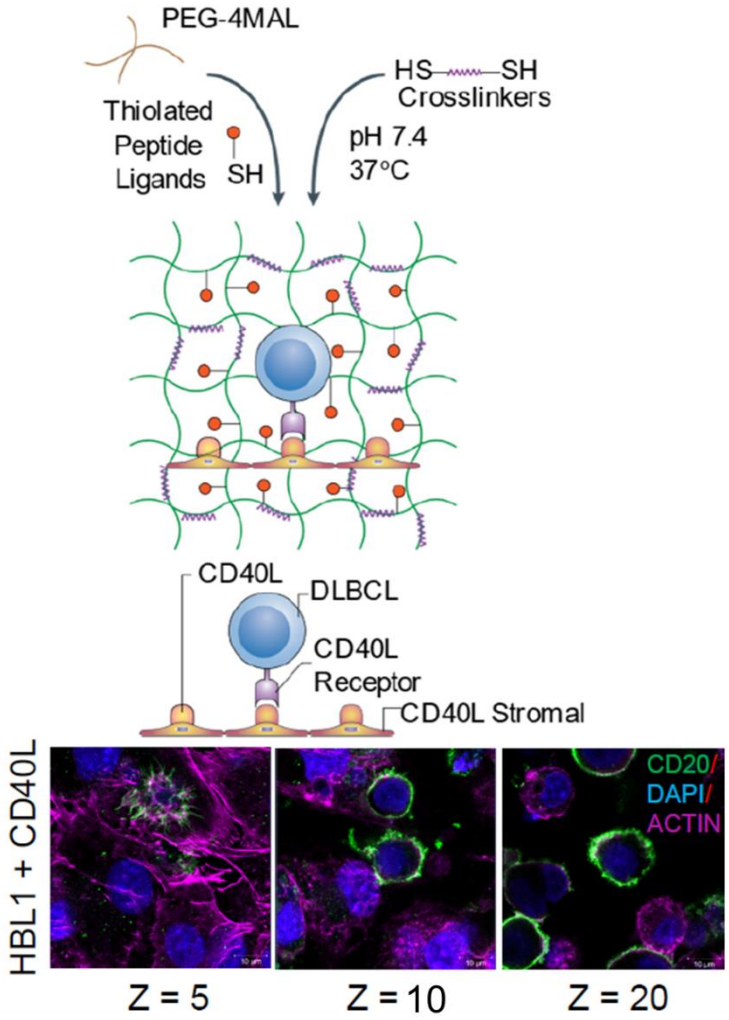

Figure 3-2: DLBCL organoids.

(Top) Schematic of PEG-4MAL hydrogel-based organoids with nondegradable and matrix metalloproteinase degradable crosslinkers (purple) functionalized with adhesive peptides (red).

Hydrogels encapsulated lymphoma cells (blue) and supporting cells (yellow). (Bottom) Confocal microscopy z-stacks of PEG-4MAL hydrogel-based organoids with ABC-DLBCL cell line HBL1 (CD20, Green), Cd40L-transduced stromal cells (Actin, spread), and nucleus (DAPI).

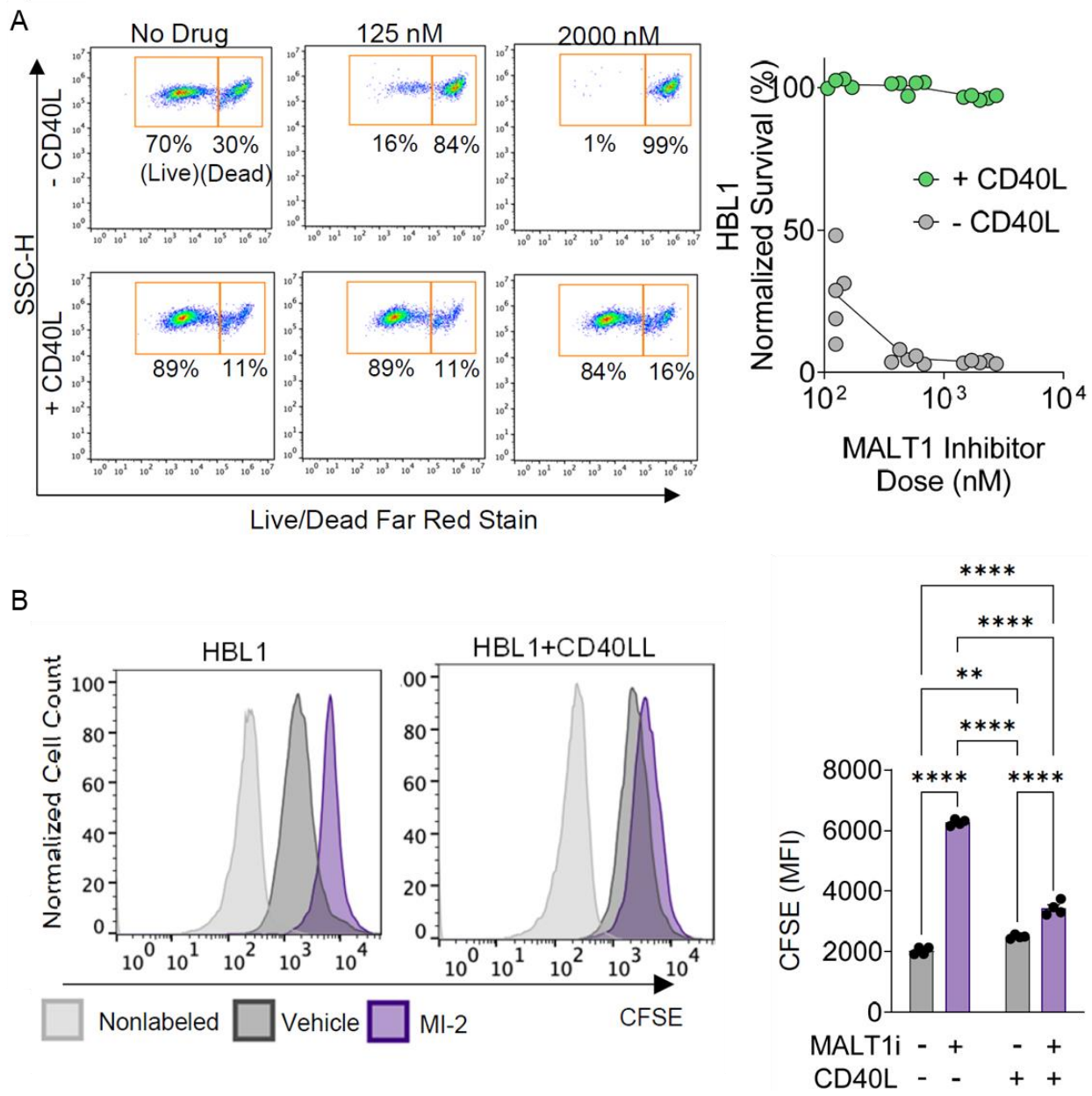

Figure 3-3: DLBCL response to MALT1 inhibitor MI2 with stromal support.

A) Left: Flow cytometry and Right: Survival (normalized to vehicle-treated) of HBL1 cells

cultured with or without CD40L-presenting cells after 48 hours of culture and subsequent 48 hours of treatment with increasing concentration of MALT1 inhibitor MI-2 in the range of 0-2000 nM (n = 5).

B) Assessment of proliferation after pre-labeling cells with CFSE and subsequent 96-hour culture, including 48-hour treatment with 2000 nM MI-2. Representative flow cytometry histograms with unlabeled cells as well as vehicle or MI-2 treated CFSE-labeled cells is on left. Quantification of CFSE for each culture condition, where results indicate the means ± SEM of 4 replicates, is on the right. Unpaired t-test, ****P<0.0001.

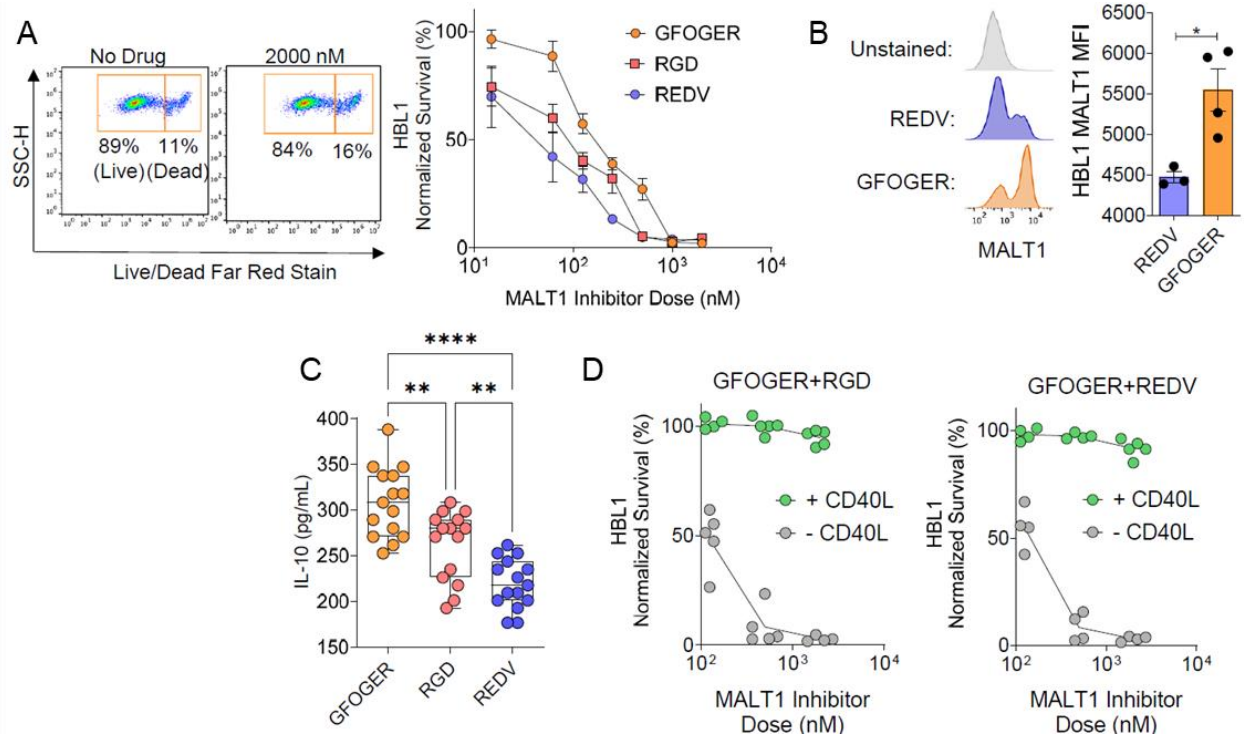

Figure 3-4: DLBCL response to MALT1 inhibitor MI2 with ECM variations.

A) Survival (normalized to vehicle-treated) of HBL1 cells normalized to vehicle-treated cultured in indicated conditions that compare GFOGER-presenting organoids to those that present REDV (left) and RGD (right) after 48 hours of culture and subsequent 48 hours of treatment with MI-2.

Results indicate the means ± SEM of 5 replicates.

B) Median fluorescent intensity of MALT1 in HBL1 cells cultured in indicated conditions for 96 hours. Unpaired t-test, *P<0.05 (n=3-4).

C) IL10 secreted from cells cultured in indicated conditions for 96 hours. 1-way ANOVA, **P<0.01, ****P<0.0001 (n = 15).

D) Survival (normalized to vehicle-treated) of ABC-DLBCL cell line HBL1 cultured in either GFOGER+REDV or GFOGER+RGD functionalized hydrogels (with or without CD40L-presenting cells) after 48 hours of culture and subsequent 48 hours of treatment with increasing concentration of MALT1 inhibitor, MI-2. Results indicate the means ± SEM of 5 replicates.

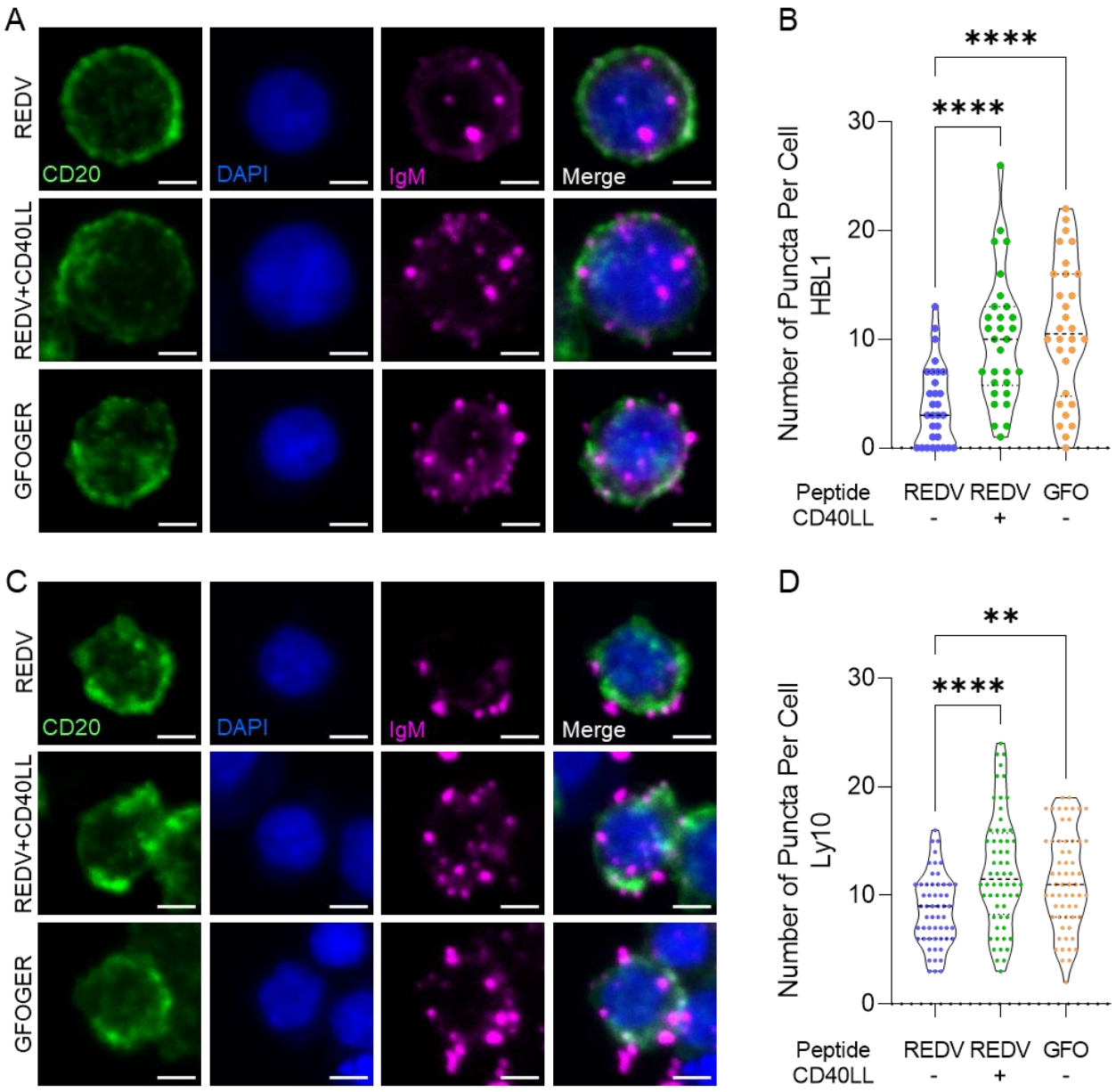

Figure 3-5: Presentation of CD40L signal and GFOGER peptide ligand boost puncta formation in DLBCLs.

A) Representative images of IgM puncta on HBL1 cells in organoids. Scale bars are 5µm.

B) Number of puncta per cell in HBL1 organoids. 6 cells were imaged per organoid in 5 organoids. 1-way ANOVA, ****P<0.0001 (n = 30).

C) Representative images of IgM puncta on Ly10 cells in organoids. Scale bars are 5µm.

D) Number of puncta per cells in Ly10 organoids. Each point represents a single cell within an organoid. 12 cells were imaged per organoid in 5 organoids. 1-way ANOVA, **P<0.01, ****P<0.0001 (n = 57-60).

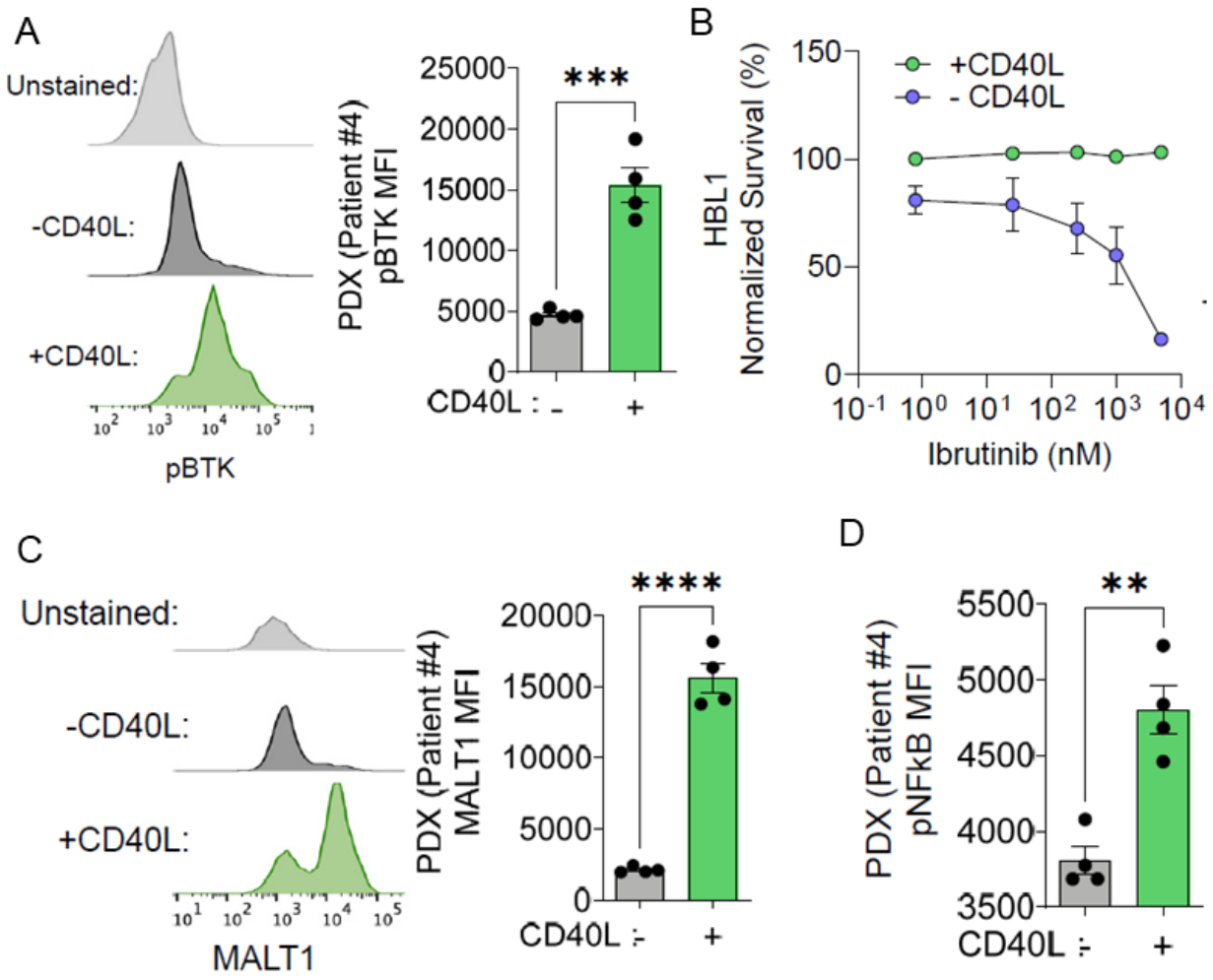

Figure 3-6: Tumor microenvironment and BCR signaling.

A) pBTK median fluorescent intensity in human PDX cells cultured in organoids with and without CD40L for 96 hours. Unpaired t-test, ***P<0.001 (n =4).

B) Survival (normalized to vehicle-treated) of human PDX cells cultured in indicated conditions after 48 hours of culture and subsequent 48 hours of treatment with increasing concentration of BTK inhibitor, Ibrutinib. Results indicate the means ± SEM of 6 replicates.

C) Median fluorescent intensity of MALT1 in human PDX cells cultured in ±CD40L stromal cell conditions for 96 hours. Unpaired t-test, ****P<0.0001 (n =4).

D) Median fluorescent intensity of pNFkB in human PDX cells cultured in ±CD40L stromal cell conditions for 96 hours. Unpaired t-test, **P<0.01 (n =4).

CHAPTER 4

Multi-mode antigen presentation for immunomodulation

4.1 Abstract

Follicular dendritic cells (FDCs) maintain germinal center architecture and play a key role in germinal center B cell selection. Here we show cellular- and bead-based models of FDC presentation of antigen to germinal center B cells. Biomaterials-based nanovaccines, such as those made of poly(lactic-co-glycolic acid) (PLGA), can induce stronger immunity than soluble antigens in healthy wild-type mouse models. However, whether metabolic syndrome can influence the immunological responses of nanovaccines remains poorly understood. Here, we first show that alteration in the sensing of the gut microbiome through Toll-like receptor 5 (TLR5) and the resulting metabolic syndrome in *TLR5*$^{-/-}$ mice diminish the germinal center immune response induced by PLGA nanovaccines. We next demonstrate that the low immune response can be rescued by an immunomodulatory Pyr-pHEMA nanogel vaccine, which functions through TLR2 stimulation, enhanced trafficking, and induced stronger germinal center response than alum-supplemented PLGA nanovaccines. To further investigate germinal center response to nanogels, we use immune organoids to show that Pyr-pHEMA nanogels induced stronger germinal center response and epigenetic activity *ex vivo*. The study highlights the potential for immunomodulation under gut-mediated metabolic syndrome conditions using advanced nanomaterials.

4.2 Introduction

Follicular dendritic cells (FDCs) are required to maintain germinal center architecture[93]. FDCs *in vivo* capture and process antigen for uptake by germinal center (GC) B cells during selection for high-affinity B cell receptors (BCRs). are mobile, membrane-based presentation of antigen for

increased antigen uptake. Using these models will improve understanding of immune cell function as well as vaccine uptake.

At a smaller scale than FDC-antigen-GC B cell interactions, mode of antigen presentation in vaccines affects vaccine uptake. Ways to improve vaccine efficacy include targeting immune tissues and using adjuvants to boost the immune response. Lymph nodes have been targeted for vaccine delivery to improve efficacy[19]. Material, size, and surface charge of vaccines are tuned to increase trafficking to lymph nodes and uptake by antigen presenting cells. Vaccine efficacy is reduced in patients with dysregulated immune systems resulting from conditions like metabolic syndrome.

Metabolic syndrome is a cluster of metabolic disorders, such as systemic inflammation, insulin resistance, and obesity[94,95]. The National Cholesterol Education Program Adult Treatment Panel III definition[96,97] is one of the most widely used criteria of metabolic syndrome and incorporates the key features of hyperglycemia/insulin resistance, visceral obesity, atherogenic dyslipidemia, and hypertension. Metabolic syndrome can originate from a variety of factors such as gut microbiome, diet, and genetic mutations, among others[98]. The gut microbiome is particularly interesting because it has been implicated as a cause of metabolic syndrome[94], and multiple lines of evidence link the gut microbiota and metabolic syndrome to the immune system and, more directly, to vaccine response[99–101]. In one example, mice deficient in Toll-like receptor 5 (TLR5, a cell surface protein that senses flagella on gut bacteria) spontaneously developed metabolic syndrome[101] and have also been shown to have a poor soluble antigen response[102]. In the latter study, soluble influenza vaccine response showed a direct correlation between expression of TLR5

and the magnitude of the antibody response. The study further showed that TLR5-mediated sensing of the microbiota also affected antibody responses to the inactivated polio vaccine. Despite these studies, it remains unclear whether the gut microbiome can regulate the response of materials-based nanovaccines, which have the potential to mount stronger immune response than soluble vaccines, even in the absence of adjuvants. It also remains unclear whether immunomodulatory nanomaterials can overcome any immune regulations imposed by gut microbiome and metabolic syndrome.

Here, we first elucidate how TLR5-mediated sensing of the microbiota and the associated metabolic syndrome modulates the immune response induced by conventional PLGA nanovaccines. We disrupted the gut microbiome sensing using *TLR5*$^{-/-}$ mice and observed that the resulting metabolic syndrome diminishes the immune response induced by conventional PLGA nanovaccines in the absence of any exogenous adjuvant. The PLGA nanovaccines show reduced particle trafficking to draining lymphoid tissues, and nanovaccines further changed the selective composition of the gut microbiota. By chronically treating WT mice with antibiotics since weaning, we show that disrupting gut signaling leads to poor vaccine response in an obesity-independent manner. We next engineer an immunomodulatory pyridine–poly(hydroxyethyl methacrylate) (Pyr-pHEMA), which self- assembles with protein antigens to form a nanogel vaccine. The Pyr-pHEMA nanogels overcome the diminished response of PLGA vaccines in the metabolic syndrome model by modulating the immune response in immune cells through TLR2 and mount B cell response higher than alum-supplemented PLGA nanovaccines. The results highlight the potential of advanced nanomaterials as immunomodulatory vaccines under gut-mediated metabolic syndrome conditions.

4.3 Cellular Presentation of Antigen

To study antigen presentation *ex vivo*, we fabricated hydrogel-based organoids to encapsulate 40LB stromal cells, B cells isolated from C57BL/6 mouse spleens, and the antigen. The hydrogel consisted of 4-arm polyethylene glycol maleimide (PEG-MAL) functionalized with REDV peptide and crosslinked with VPM and DTT. We presented 4-hydroxy-3-nitrophenylacetyl-ovalbumin (NP-OVA) antigen on the surface of follicular dendritic cells, HK, using a biotinylated HLA antibody and streptavidin conjugation (Figure 4-1A-B). Surface NP-OVA was present on stromal cells on day 0, but by day 4 was no longer present. HK-NP-OVA boosted the number of activated B cells ($GL7^{+}CD19^{+}$) in organoids compared to soluble NP-OVA only, and was similar to HK with soluble NP-OVA (Figure 4-1C). This suggests that the presence of HK increased the activated B cell numbers rather than cell membrane presentation of antigen. HK cells lost surface NP-OVA by day 4, but FDCs *in vivo* are able retain antigen for long periods of time. Therefore we decided to use more persistent presentation of antigen in the organoids, we moved to a bead-based system.

4.4 Bead Presentation of Antigen

We conjugated NP-OVA to 5 μm polystyrene beads using a streptavidin-biotin reaction (Figure 4-2A). NP was present on the surface of the beads throughout the duration of culture in organoids (Figure 4-2B). Bead-based presentation of NP-OVA increased the number of NP-specific germinal center-like cells compared to soluble NP-OVA or no antigen (Figure 4-2C). This suggests that antigen specificity of B cells can be improved with the use of polystyrene beads due to the mode of antigen uptake.

4.5 PLGA Nanovaccines Mount Limited Immunity Under Gut-Mediated Metabolic Syndrome in Mice[ii]

We examined whether altered sensing of the gut microbiome and the resulting metabolic syndrome regulate the success of a model PLGA nanovaccine, which is among the most widely used nanovaccine platforms[103,104]. Mice were immunized subcutaneously either with PLGA nanovaccines formulated with 50 μg of 4-hydroxy-3-nitrophenyl acetyl hapten conjugated to ovalbumin (NP-OVA) or as a soluble NP-OVA antigen. Previous studies have shown that mice immunized with soluble NP-OVA antigen induce NP-specific immune response[105]; therefore, our experimental design did not initially include additional adjuvants to better understand the efficacy of PLGA nanovaccines. Thirty-five days later[37,103], a booster dose was injected, and after another 10 days, cells were harvested from the spleen and the draining lymph node. Nanovaccines induced significantly higher $GL7^+FAS^+CD19^+$ germinal center B cells in the lymph node after immunization as compared to soluble NP-OVA (Figure 4-3A). In contrast, there was no difference in the vaccine response between soluble NP-OVA–injected *TLR5*$^{-/-}$ and nanovaccine-injected *TLR5*$^{-/-}$ mice.

We quantified $CD138^+$ plasma cells in draining lymph nodes and observed a trend similar to that of the germinal center response (Figure 4-3B). The antigen-specific immunoglobulin G (IgG) antibodies in the blood serum increased 2.5- to 3.5-fold in WT mice but not in *TLR5*$^{-/-}$ mice, further confirming that only the WT mice gained the benefits associated with PLGA vaccination, when compared to the soluble antigen (Figure 4-3C).

[ii] Sections 4.5-4.7 was published in [124]Mosquera, …, Lai et al., *Science Advances* 2019

4.6 Immunomodulatory Nanogel Mode of Stimulation

It is well established that materials or biologics that mimic bacterial pathogen-associated molecular patterns are capable of stimulating TLRs on the surface of immune cells. In a competing theory by Seong and Matzinger[106], hydrophobic portions of biological molecules and potentially materials can act as universal damage-associated molecular patterns to initiate an immune response, in particular through TLR2 and TLR4[107–110]. New studies have shown that select small-molecule compounds that are aromatic in nature and structurally unrelated to any known TLR2 agonists can function as TLR2 agonists[108]. Since Pyr-pHEMA has hydrophobic pyridine attached to pHEMA and pyridine is an aromatic compound, we next investigated whether Pyr-pHEMA nanogel would stimulate immune cells either through TLR2 or TLR4 or, alternatively, through TLR5 or TLR9. We transfected TLR2, TLR4, or TLR9 into human embryonic kidney (HEK) 293 cells (that endogenously express TLR5) and exposed the cells to Pyr-pHEMA nanogels carrying NP-OVA antigen (20 μg/ml), antigen alone (20 μg/ml), or media. Pyr-pHEMA nanogels stimulated TLR2 signal, as indicated by high relative light units of luciferase (Figure 4-4A), but had minimal effect on TLR4, TLR5, and TLR9, similar to antigen alone and media. These results suggest that Pyr-pHEMA nanogels function through TLR2 (Figure 4-4B) and that the stimulation is driven by polymer and not the complexed protein. We tested this hypothesis by comparing immune response in *TLR2*$^{-/-}$, *TLR4*$^{-/-}$, and WT mice (Figure 4-4C). Previous studies[111] have shown that the small intestinal TLR5 expression is not regulated through TLR2 or TLR4, as shown by unchanged levels of small intestinal TLR5 transcript in small intestinal tissues of *TLR2*$^{-/-}$ and *TLR4*$^{-/-}$ mice. These studies further showed that *TLR5*$^{-/-}$ mice did not affect TLR2 and TLR4 mRNA levels. Therefore, we do not expect TLR5 to be influenced in TLR2 and TLR4 mice.

4.7 Immunomodulatory Nanogels in Murine Model of Gut-Mediated Metabolic Syndrome

We immunized *TLR2*$^{-/-}$, *TLR4*$^{-/-}$, and WT mice with NP-OVA as a soluble antigen or formulated with Pyr-pHEMA nanogel. We observed that while both WT and *TLR4*$^{-/-}$- deficient mice had significantly elevated $GL7^+FAS^+CD19^+$ germinal center B cell population relative to their soluble counterparts, *TLR2*$^{-/-}$- deficient mice did not experience any increase in humoral immunity relative to the soluble antigen.

We immunized male *TLR5*$^{-/-}$ mice either with Pyr-pHEMA nanogels formulated with 50 μg of NP-OVA or as a soluble antigen to determine whether the nanogel would boost the immune response beyond the soluble formulation. Ten days after the booster dose, Pyr-pHEMA nanogels induced a significant 1.5-fold higher $GL7^+FAS^+CD19^+$ germinal center B cells in the lymph node as compared to soluble NP-OVA (Figure 4-5A). This is in contrast with PLGA vaccines (Figure 4-3), suggesting that Pyr-pHEMA can rescue the poor immune response in the male *TLR5*$^{-/-}$ mouse model. Analysis of $CD138^+$ cells unveiled a similar trend, and the Pyr-pHEMA response was comparable in *TLR5*$^{-/-}$ and WT mice (Figure 4-5B). The antigen-specific antibodies in the blood serum confirmed that engineered Pyr-pHEMA nanogel rescued the limited immune response shown in PLGA nano- vaccines as compared to the soluble antigen (Figure 4-5C).

As indicated in Figure 4-5D, addition of alum to PLGA nanovaccines rescued the B cell response in *TLR5*$^{-/-}$ mice to the level of WT mice immunized with PLGA nanovaccines alone. In contrast, Pyr-pHEMA nanogels without any exogenous adjuvant induced higher germinal center response in *TLR5*$^{-/-}$ mice as compared to alum-supplemented PLGA nanovaccines. Therefore, Pyr-pHEMA nanogels offer an immunomodulatory effect without the combinatorial delivery of adjuvants.

4.8 H1N1 Pyr-pHEMA Nanogel Formulation

The studies presented above showed that pyr-pHEMA nanogels boosted germinal center cell numbers *in vivo*. However, these studies used model antigen NP-OVA, and we wanted use complex antigens such as H1N1. We wanted to test how direct interactions between pyr-pHEMA nanogels and B cells affected germinal center response *ex vivo*. We hypothesized that pyr-pHEMA nanogels would increase the number of germinal center-like cells in immune organoids. Pyr-pHEMA and inactivated H1N1 were mixed to form self-assembly nanogels (Figure 4-6A). Nanoparticles <200 nm can traffic through lymph nodes to encounter B cells[112]. We decided to use the formulation that yielded an average size of 240.0±96.9 nm (Figure 4-6B). The loading efficiency of H1N1 as measured by ELISA was >90% (Figure 4-6C).

4.9 Germinal Center Response to H1N1 Nanogels

Comparing soluble H1N1 to lower dose of nanogel H1N1, the lower dose of nanogel H1N1 still had higher numbers of $GL7^{+}CD19^{+}$ activated B cells than a higher dose of soluble H1N1 (Figure 4-6D). We tested a lower dose of H1N1 and found similar response, where nanogel H1N1 had higher numbers of germinal center-like B cells than soluble H1N1 (Figure 4-6E). Enhancer of zeste homolog 2 (EZH2) is a histone methyltransferase that silences genes by catalyzing histone 3 lysine 27 trimethylation (H3k27me3). EZH2 is required for germinal center formation[37]. CDKN1A stops cell cycle progression, so EZH2-mediated silencing of CDKN1A allows for progression of cycle, which in turn allows for germinal center formation. We measured EZH2 expression levels and found no significant differences, but its epigenetic activity by H2k27me3 had increased expression levels, indicating higher epigenetic activity (Figure 4-6F,G).

4.10 Pyr-pHEMA NP-OVA Nanogels in Organoids

We wanted to determine whether the boost in immune response was due to the pyr-pHEMA polymer itself, or the nanogel presentation of antigen. We moved back to using NP-OVA as the antigen because we did not want the highly immunogenic H1N1 to mask the effects of pyr-pHEMA in nanogels. We found that nanogel NP-OVA increased the number of activated B cells over both unassembled pyr-pHEMA and soluble NP-OVA, which indicated that higher activation of B cells was due to nanogel presentation of NP-OVA rather than polymer alone (Figure 4-7A). Nanogel NP-OVA also increased the number of $EZH2^{+}CD19^{+}$ cells and $H3k27me3^{+}EZH2^{+}CD19^{+}$ over soluble NP-OVA (Figure 4-7C-D). EZH2 expression was higher in nanogel NP-OVA groups than soluble NP-OVA groups (Figure 4-7C). The expression levels of H3k27me3 in nanogel NP-OVA samples were not higher than in soluble NP-OVA samples, indicating that nanogels did not boost epigenetic activity of EZH2 (Figure 4-7D).

4.11 Intravital 3-Photon Imaging of Murine Lymph Node

Cγ1Cre-Confetti mice[113,114], in which B cells in the germinal center (GC) stochastically express one or two of four different fluorescent proteins (CFP in membrane, GFP in nucleus, YFP and RFP in cytoplasm), providing 10 color combinations. We used 3-photon microscopy to image GC B cells *in vivo*. Using 1300 nm excitation and 3 detection channels we visualized multi-color GC B cells 8-10 days after mice immunization with NP-OVA in alum (Figure 4-8A,B). The GFP and YFP signals were detected by the same detection channel, as their spectral separation is small. We could distinguish 7 color combinations because GFP/RFP was distinguishable from YFP/RFP. To distinguish the light zone (LZ) and dark zone (DZ) in the GC, we labeled the follicular dendritic cells in the LZ with an Alexa Fluor 594-counjugated CD35 antibody (Figure 4-8A). Intravital 2PM

has been used before to image the GCs in the popliteal LN[115,116], as most GCs are in the shallow region of the popliteal LN in the cortical side. However, it is challenging to reach the bottom of large GC (DZ thickness ~100 μm) by 2PM. The lower part of GC DZ at 250-300 μm depth in popliteal LN imaged by 890 nm 2PM was blurry, while the entire GC was clearly visible by 1300 nm 3PM (Figure 4-8A,B).

4.12 Materials and Methods

4.12.1 Cell Culture

40LB was cultured in Dulbecco's Modified Eagle Medium supplemented with 10% fetal bovine serum and 1% penicillin/streptomycin.

4.12.2 Cell Membrane Presentation of Antigen

HK cells were incubated with a biotin anti-HLA-ABC antibody (Biolegend). NP-OVA was functionalized with streptavidin using a Lightning-Link Streptavidin Conjugation Kit (Novus) according to manufacturer's instructions. HK with biotin anti-HLA-ABC antibody was then washed and incubated with streptavidin-NP-OVA for 1 hr.

4.12.3 Particle-Based Presentation of Antigen

5 μm biotin functional polystyrene beads (Nanocs) were incubated with streptavidin-NP-OVA for 1 hr at room temperature, centrifuged, and washed with PBS.

4.12.4 Organoid Fabrication

7.5% weight/volume 4-arm PEG-MAL (20 kDa) hydrogels were fabricated according to

previously reported methods. Briefly, one out of four arms of PEG-MAL (Laysan Bio) were functionalized with thiolated peptide G**REDV**GC (Aapptec), and the remaining arms were crosslinked using a 50%/50% mixture of MMP9 degradable GCRD**VPM**SMRGGDRCG (Aapptec) and nondegradable dithiothreitol (DTT) (Invitrogen). All components were reconstituted in 1% HEPES buffer. 40LB cells were treated with mitomycin C for 45 minutes and washed twice with PBS. B cells were isolated from WT C57BL/6J or B6.129P2-Ptprc<a> Igh<tm1Mnz>/J (B1-8) mouse spleens using EasySep Mouse B Cell Isolation Kit (StemCell Technologies) according to the manufacturer's instructions. Organoids were cultured in Rosewell Park Memorial Institute (RPMI) 1640 supplemented with 10% fetal bovine serum and 1% penicillin/streptomycin.

4.12.5 Mouse Studies

Mice were immunized either subcutaneously or intraperitoneally with 50 μg of NP-OVA encapsulated into pyr-pHEMA, a dose-matched soluble formulation (50 μg/mL), or PBS. For Pyr-pHEMA, *TLR5*$^{-/-}$ mice were intraperitoneally immunized either with nanovaccines formulated with 50 μg of NP-OVA or as a soluble antigen to determine whether the nanogel would boost the response beyond the soluble formulation. Previous work has shown that subcutaneous, intramuscular, and intraperitoneal injections all elicit a strong immune response in engineered vaccines; however, intraperitoneal vaccination has a shorter timeline for induction of immune response[117,118]. Two weeks later, a booster dose was injected, and after another 10 days, cells were harvested from the draining lymph node. Similar studies were performed with *TLR2*$^{-/-}$, *TLR4*$^{-/-}$, and WT mice with matched age and gender. For 3-photon imaging of mouse popliteal lymph nodes, NP-OVA with adjuvant Imject Alum (Thermo Scientific), which contains an aqueous

solution of aluminum hydroxide (40 mg/mL) and magnesium hydroxide (40 mg/mL) plus inactive stabilizers, were prepared as per the manufacturer's recommendation. Briefly, Imject Alum was added dropwise with constant mixing to the NP-OVA so that the final volume ratio of Imject Alum to immunogen was 1:1 and injected into mouse footpad. All animal studies were performed in compliance with the Institutional Animal Care and Use Committee (IACUC) at Cornell University.

For *in vivo* GC B cell imaging, Cγ1Cre-Confetti mice were generated by mating Cγ1-cre mice ((B6.129P2(Cg)-Ighg1tm1(cre)Cgn/J, The Jackson Laboratory) with R26R573 Confetti mice (Gt(ROSA)26Sortm1(CAG-Brainbow2.1)Cle/J, The Jackson Laboratory). For immunization of the Cγ1Cre-Confetti mice, we injected 50 μL of the mixture of NP-OVA (2mg/ml in PBS, N-5051, Biosearch Technologies) and alum at a 1:1 volume ratio into the footpad of the mouse. To label follicular dendritic cells in the popliteal LN, we injected 2 μg CD35 antibody (558768, BD Bioscience) conjugated with Alexa Fluor 594 (A20185, Thermo Fisher) into the footpad of the mouse about 12 hours before the imaging.

4.12.6 Pyr-pHEMA Polymer Synthesis

Nicotinoyl chloride hydrochloride was dissolved in tetrahdydrofuran (THF). A mixture of polyhydroxyethylmethacrylate (pHEMA) and 4-dimethylaminopyridine (DMAP) was dissolved in THF. pHEMA/DMAP was added to the nicotinoyl chloride hydrochloride dropwise. The reaction was allowed to continue overnight. The mixture was transferred to a tube and centrifuged. The THF solvent portion was collected and the powder at the bottom was discarded. Th solvent was allowed to evaporate, leaving a solid in the tube. The solid products were dissolved in dichloromethane (DCM), washed with DI water and brine. The DCM portion was extracted and

allowed to fully evaporate. The remaining solid was reconstituted in DCM. The product was crashed out by adding the DCM solution to cold ether. The product was further washed with cold ether. Ether was allowed to evaporate to leave the pyr-pHEMA product.

4.12.7 Nanogel Assembly, Size Characterization, and Loading Efficiency

Nanogels were formed by adding 0.2 mL of 0.2 mg mL-1 pyridine-pHEMA in dimethylformamide to protein solution. Protein solutions were 100 and 200 μg mL^{-1} H1N1 antigen and 1, 10, and 100 μg mL^{-1} NP-OVA. Size distribution of nanogels was characterized on NanoSight at the Cornell Nanoscale Science and Technology Facility. Loading efficiency was determined by using ELISA to measure hemagglutinin concentrations in the H1N1 antigen solution before nanogel assembly and supernatant after centrifugation of nanogels, taking the difference, and dividing by the concentration before nanogel assembly.

4.12.8 Flow Cytometric Analysis

For organoids, after 4 days in culture, cells were extracted by washing organoids in PBS and incubating organoids in 125 U/mL collagenase type I in serum-free RPMI for 1 hr at 37°C. Hydrogel mixture was filtered through 60 μm filter plate (Sigma) to get cell suspension. Cells were washed and stained in FACS buffer. Antibodies used for staining were NP-AF647 (Novus), GL7-AF488, CD19-PE-Cy7, and EZH2-eFluor660 (Thermo Fisher).

Antibodies used for staining include GL7-AF488, CD19-PE-C7, FAS-APC, H3k27me3-AF488, EZH2-eFluor660, NP-AF647, and B220-PE-Cy7. Flow cytometry samples were run on a BD Accuri C6. Analysis was performed on Flowjo.

4.13 Acknowledgements

The authors acknowledge partial financial support from the NIH and NIAID (1R01AI132738-01A1 to A.S.) and the NSF CAREER Award (award no. 1554275 to A.S.).

4.14 Figures

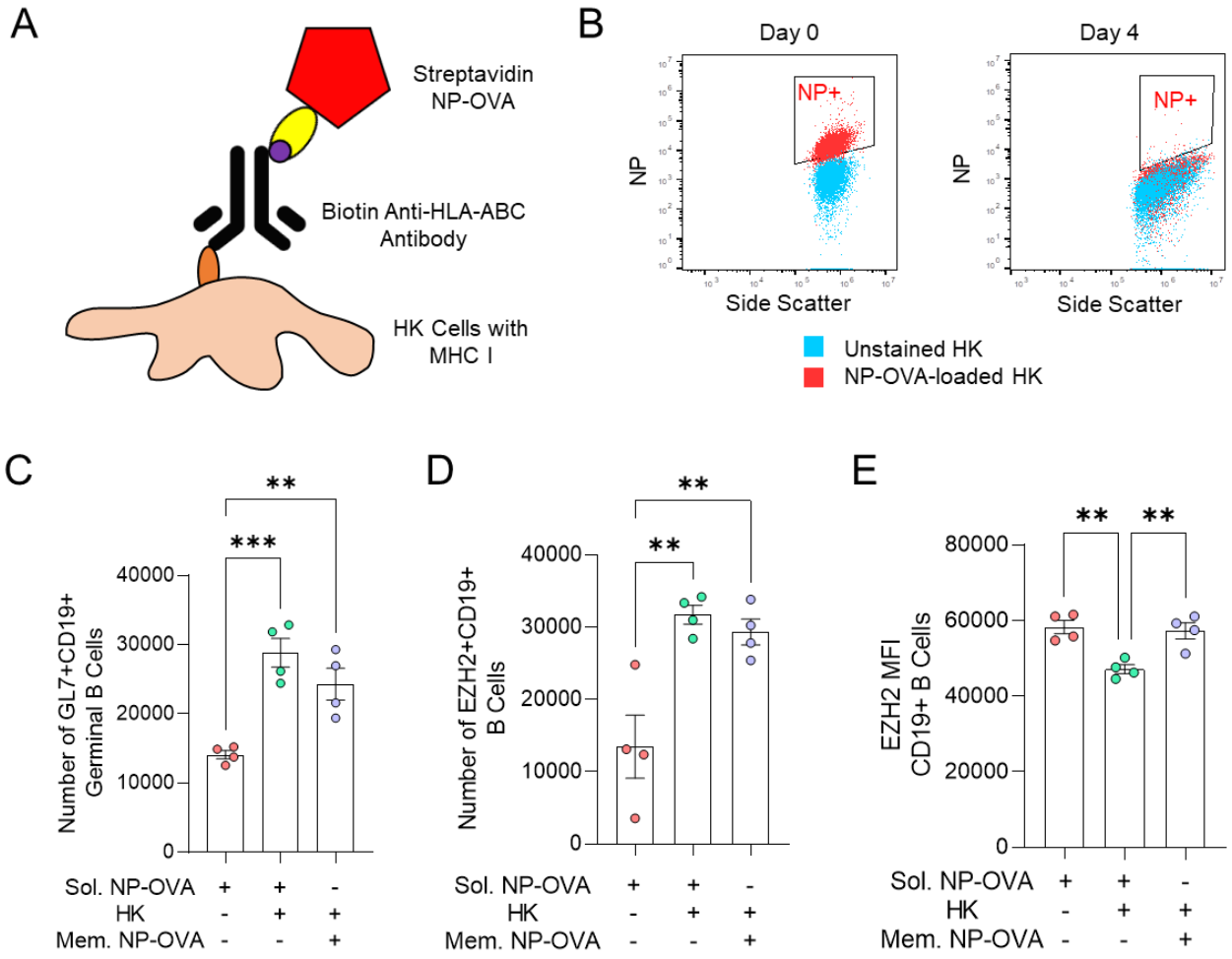

Figure 4-1: Cellular and bead-based presentation of antigen affects B cell antigen specificity.

A) Follicular dendritic cells HK with surface NP-OVA.

B) Gating of NP staining on stromal cells on days 0 and 4.

C) Number of activated B cells from organoids with HK-NP-OVA.

D) Number of B cells expressing epigenetic indicator EZH2.

E) Expression of EZH2 in B cells from organoids with HK-NP-OVA. All groups were mean ± S.E.M., compared with one-way ANOVA with Tukey's posthoc multiple comparisons test (n = 4). **p < 0.01, ***p < 0.001

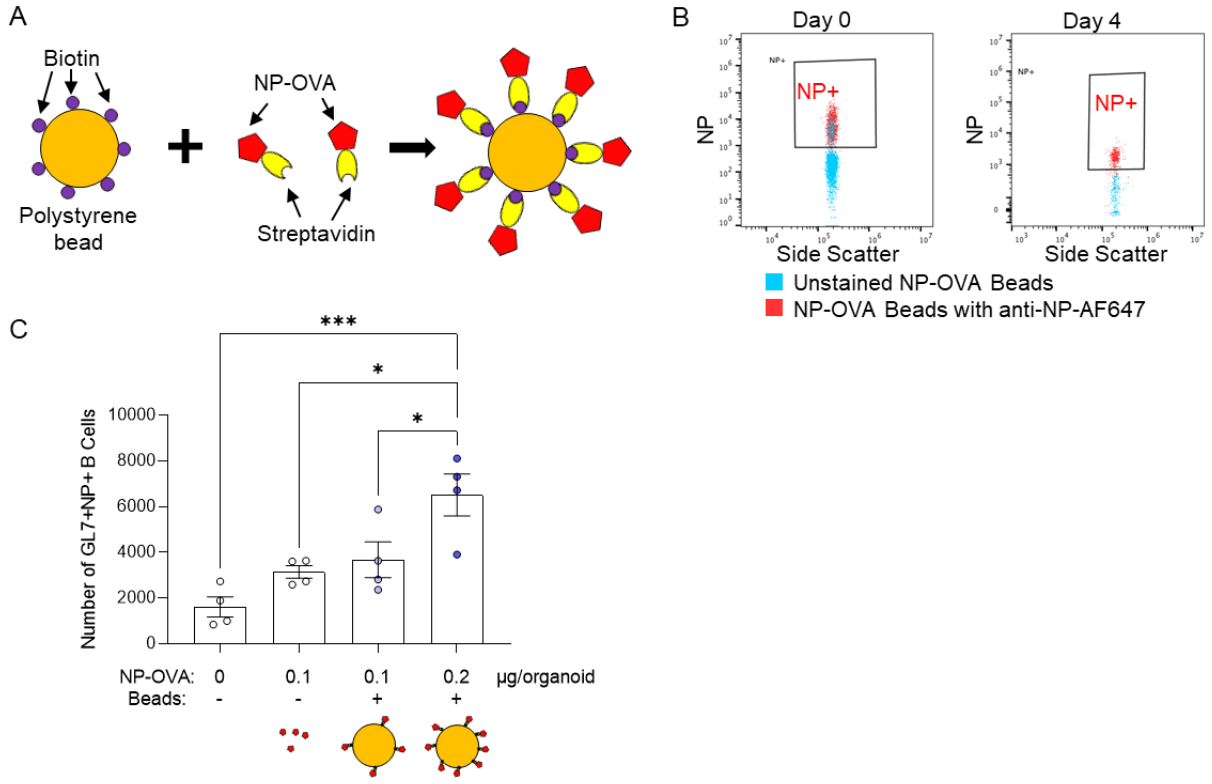

Figure 4-2: Bead-based presentation of antigen.

A) 5 µm biotin beads with streptavidin NP-OVA.

B) Gating of NP staining on NP-OVA beads on days 0 and 4.

C) Number of NP-specific activated B cells from organoids with NP-OVA beads. Mean ± S.E.M., one-way ANOVA with Tukey's posthoc multiple comparisons test (n = 4). *p < 0.05, ***p < 0.001

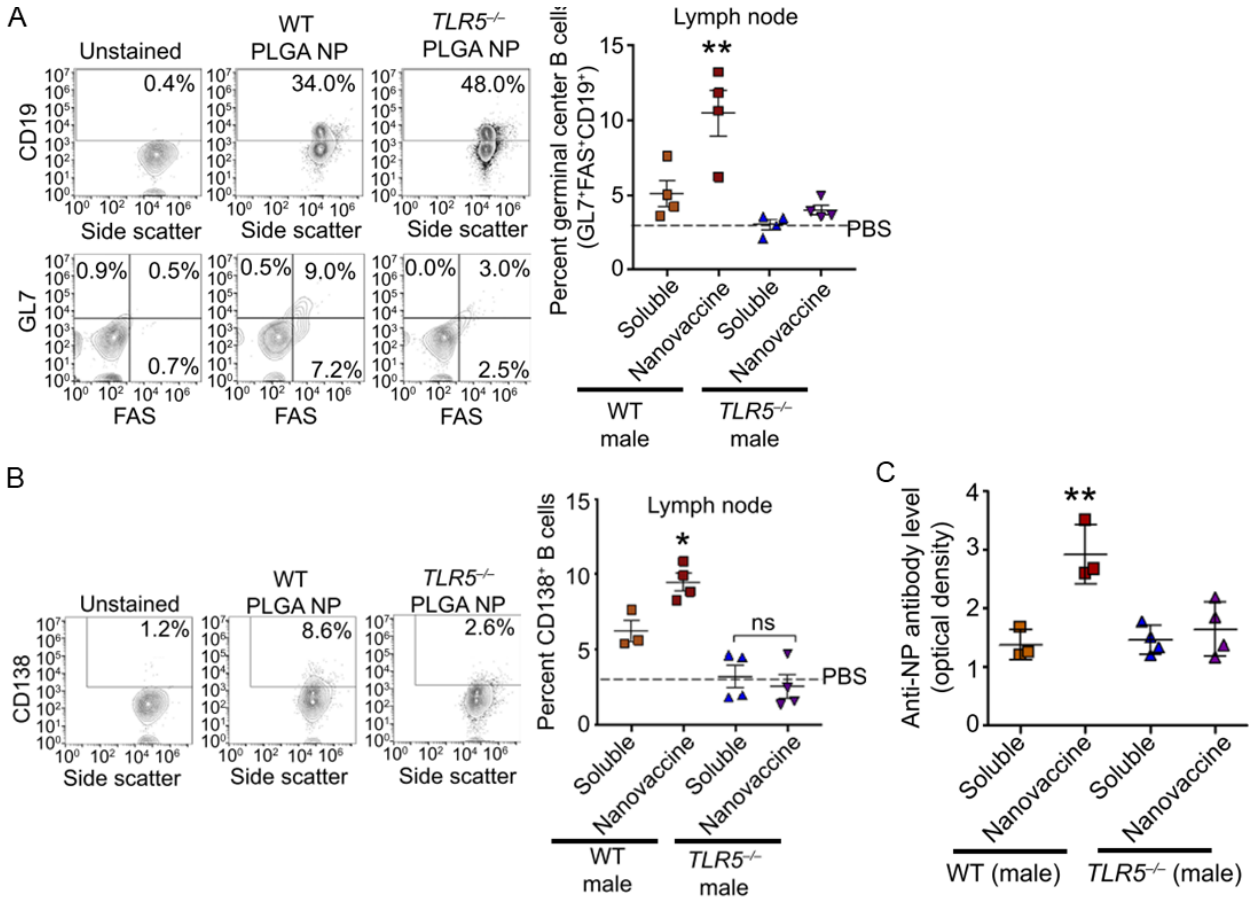

Figure 4-3: PLGA nanovaccines manifest limited humoral immune response in male *TLR5*$^{-/-}$ mice.

A) Gating strategy for GL7^{+}FAS^{+}CD19^{+} Scatterplot presents the percentage of GL7^{+}FAS^{+}CD19^{+} germinal center B cells in the lymph node of male mice 10 days after booster vaccination with either soluble NP-OVA (4-hydroxy-3-nitrophenylacetyl hapten conjugated to ovalbumin) antigen or PLGA nanovaccines formulated with NP-OVA. PBS, phosphate-buffered saline; FAS, fatty acid synthase.

B) Gating strategy for CD138^{+} plasma cells. The scatterplot presents the percentage of CD138^{+} plasma cells in the lymph node after booster vaccination.

C) The scatterplot presents the antigen-specific antibodies in the serum of male mice after immunization. Statistics was performed using an unpaired, two-tailed t test (n = 3). In all studies,

*P < 0.05 and **P < 0.01. ns denotes nonsignificant differences. MFI, mean fluorescence intensity.

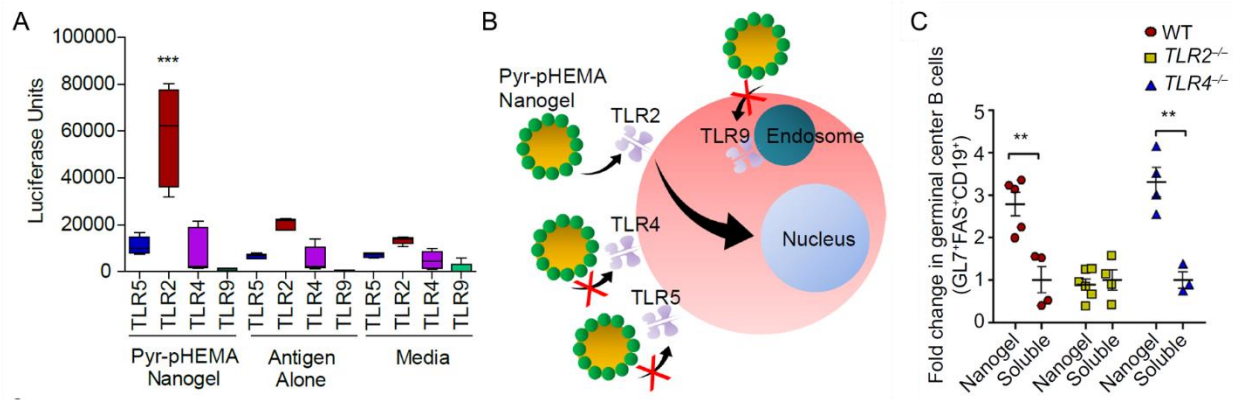

Figure 4-4: Immunomodulatory nanogels stimulate TLR2.

A) TLR stimulatory activity of Pyr-pHEMA nanogels and controls in HEK293 cells transfected with TLR2, TLR4, and TLR9. HEKs endogenously express TLR5. Luciferase activity indicates activation of a TLR. Statistics was performed using a two-way ANOVA with Bonferroni's correction (n = 5).

B) Schematic presenting the proposed hypothesis that Pyr-pHEMA nanogels function through TLR2.

C) Fold change in $GL7^+FAS^+CD19^+$ germinal center B cell population between nanogel and soluble formulations. All nanogel groups were compared by an unpaired, two-tailed t test with their soluble counterparts, and data are presented as means ± SEM (n = 5 WT nanogel, n = 4 WT soluble, n = 6 *TLR2*$^{-/-}$ nanogel, n = 5 *TLR2*$^{-/-}$ soluble, n = 4 *TLR4*$^{-/-}$ nanogel, and n = 3 *TLR4*$^{-/-}$ soluble). In all the studies, *P < 0.05, **P < 0.01, and ***P < 0.001.

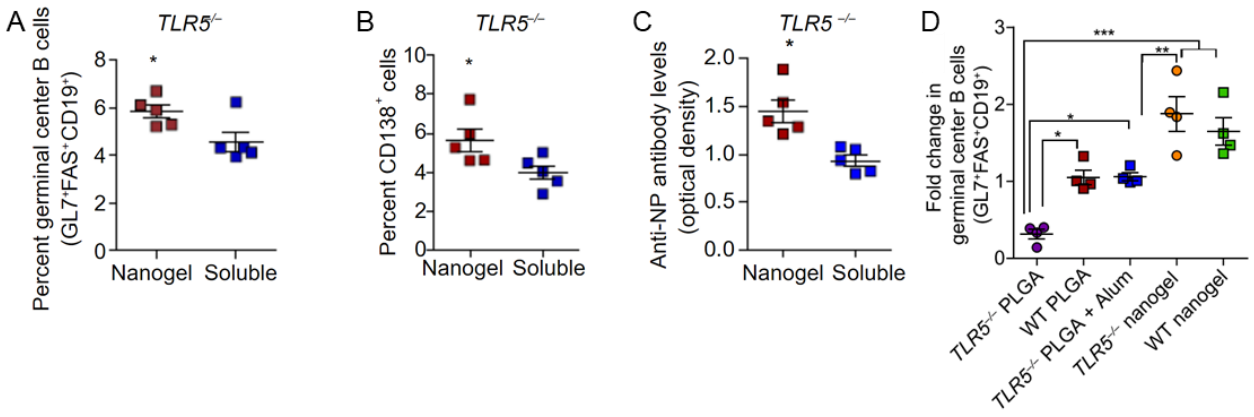

Figure 4-5: Pyr-pHEMA nanogels rescue the antigen-specific germinal center response in male TLR5$^{-/-}$ mice.

A) Pyr-pHEMA nanogel induced germinal center B cell population.

B) CD138^{+} population.

C) Antigen-specific antibody levels in the serum

D) Fold change in GL7^{+}FAS^{+}CD19^{+} germinal center B cell population between Pyr-pHEMA nanogel, PLGA nanovaccines, and PLGA nanovaccines adjuvanted with alum. All particles were loaded with NP-OVA antigen. All groups were compared by one-way ANOVA with Tukey's post hoc test, and data are presented as means ± SEM (n = 4). In this study, *P < 0.05, **P < 0.01, and ***P < 0.001.

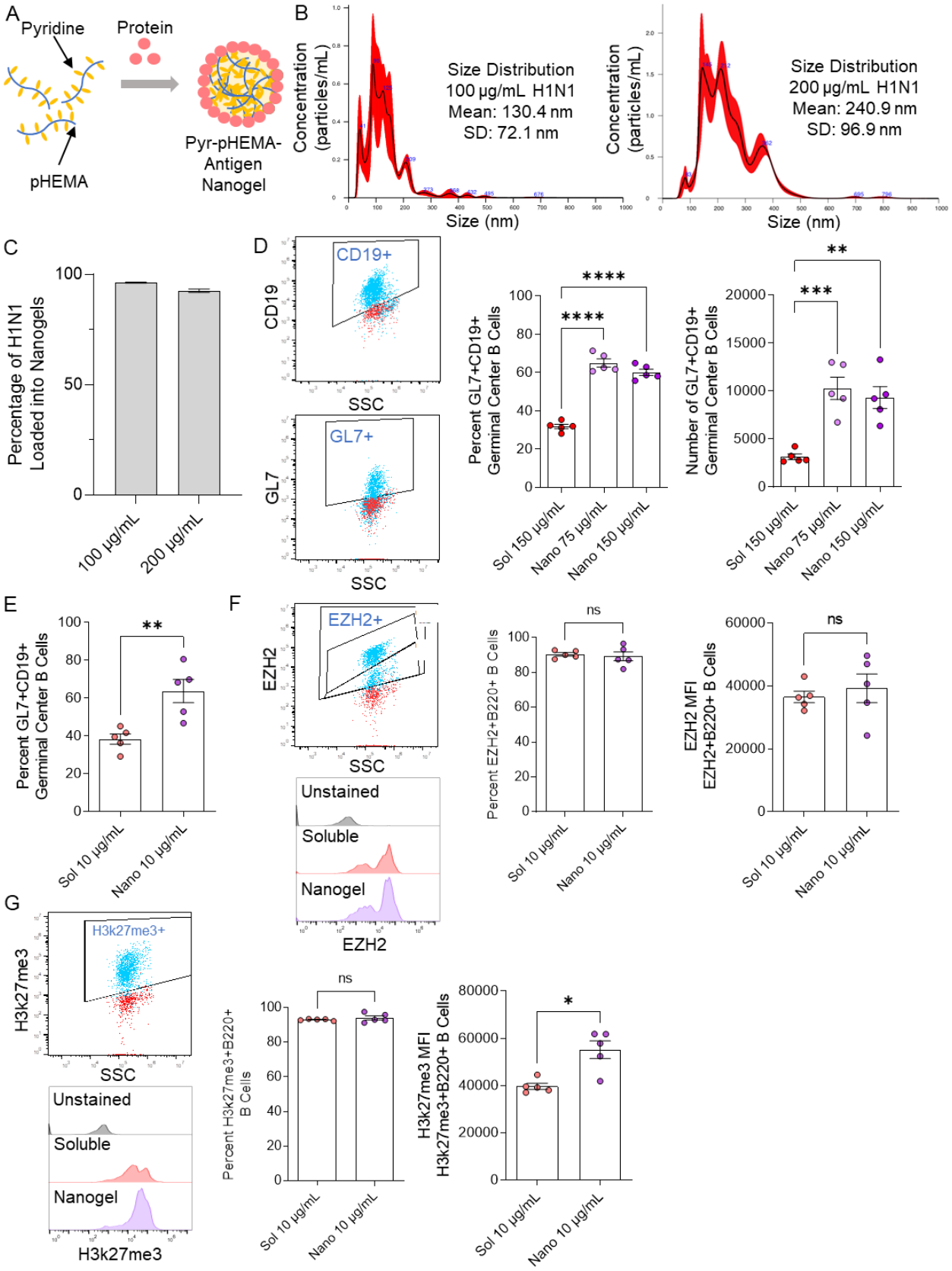
A
Pyridine
Protein
pHEMA
Pyr-pHEMA-Antigen Nanogel
B
Concentration (particles/mL)
Size Distribution
100 µg/mL H1N1
Mean: 130.4 nm
SD: 72.1 nm
Size (nm)
Concentration (particles/mL)
Size Distribution
200 µg/mL H1N1
Mean: 240.9 nm
SD: 96.9 nm
Size (nm)
C
Percentage of H1N1 Loaded into Nanogels
100 µg/mL
200 µg/mL
D
CD19+
CD19
SSC
GL7+
GL7
SSC
Percent GL7+CD19+ Germinal Center B Cells
****
****
Sol 150 µg/mL
Nano 75 µg/mL
Nano 150 µg/mL
Number of GL7+CD19+ Germinal Center B Cells
**
***
Sol 150 µg/mL
Nano 75 µg/mL
Nano 150 µg/mL
E
Percent GL7+CD19+ Germinal Center B Cells
**
Sol 10 µg/mL
Nano 10 µg/mL
F
EZH2+
EZH2
SSC
Unstained
Soluble
Nanogel
EZH2
Percent EZH2+B220+ B Cells
ns
Sol 10 µg/mL
Nano 10 µg/mL
EZH2 MFI
EZH2+B220+ B Cells
ns
Sol 10 µg/mL
Nano 10 µg/mL
G
H3k27me3+
H3k27me3
SSC
Unstained
Soluble
Nanogel
H3k27me3
Percent H3k27me3+B220+ B Cells
ns
Sol 10 µg/mL
Nano 10 µg/mL
H3k27me3 MFI
H3k27me3+B220+ B Cells
*
Sol 10 µg/mL
Nano 10 µg/mL

Figure 4-6: Germinal center response to H1N1 nanogels in immune organoids.

A) Self-assembly of pyr-pHEMA and protein into nanogel.

B) Size distribution of nanogels from NanoSight.

C) Loading efficiency of nanogels measured by hemagglutinin ELISA.

D) Representative gating for CD19 and GL7 for B cells in organoids. Percent and number of germinal center B cells with high dose of H1N1. 1-way ANOVA test. **P<0.01, ***P<0.001, ****P<0.0001

E) Number of germinal center B cells with lower dose of H1N1. Unpaired t-test. **P<0.01

F) Representative gating for EZH2. Percent $EZH2^+$ cells and EZH2 expression. Unpaired t-test. ns denotes non-significant.

G) Representative gating for H3k27me3. Percent $H3k27me3^+$ cells and H3k27me3 expression. Unpaired t-test. *P<0.05, ns denotes non-significant

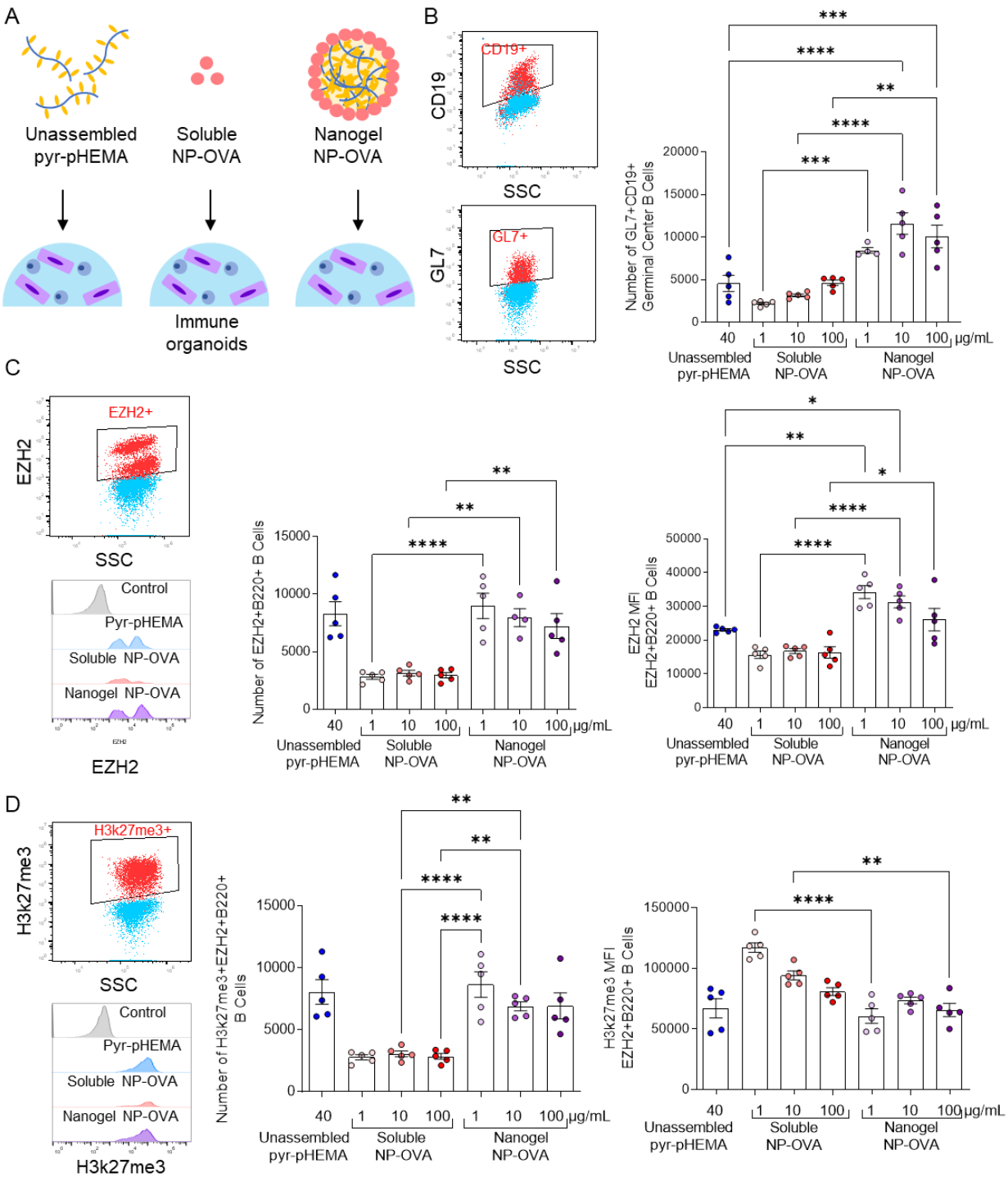

Figure 4-7: B1-8 NP-OVA nanogels

A) Media conditions for organoids. Unassembled pyr-pHEMA dissolved in DMSO, soluble NP-OVA, and nanogel NP-OVA.

B) Representative gating for CD19 and GL7, and number of activated B cells in organoids. 1-way ANOVA test.

C) Epigenetic response of EZH2. Number of $EZH2^{+}B220^{+}$ B cells and expression of EZH2.

D) Epigenetic activity through H3k27me3. Number of $H3k27me3^{+}EZH2^{+}B220^{+}$ B cells and expression of H3k27me3. All groups were compared using one-way ANOVA test. **p<0.01, **p<0.01, ***p<0.001, ****p<0.0001

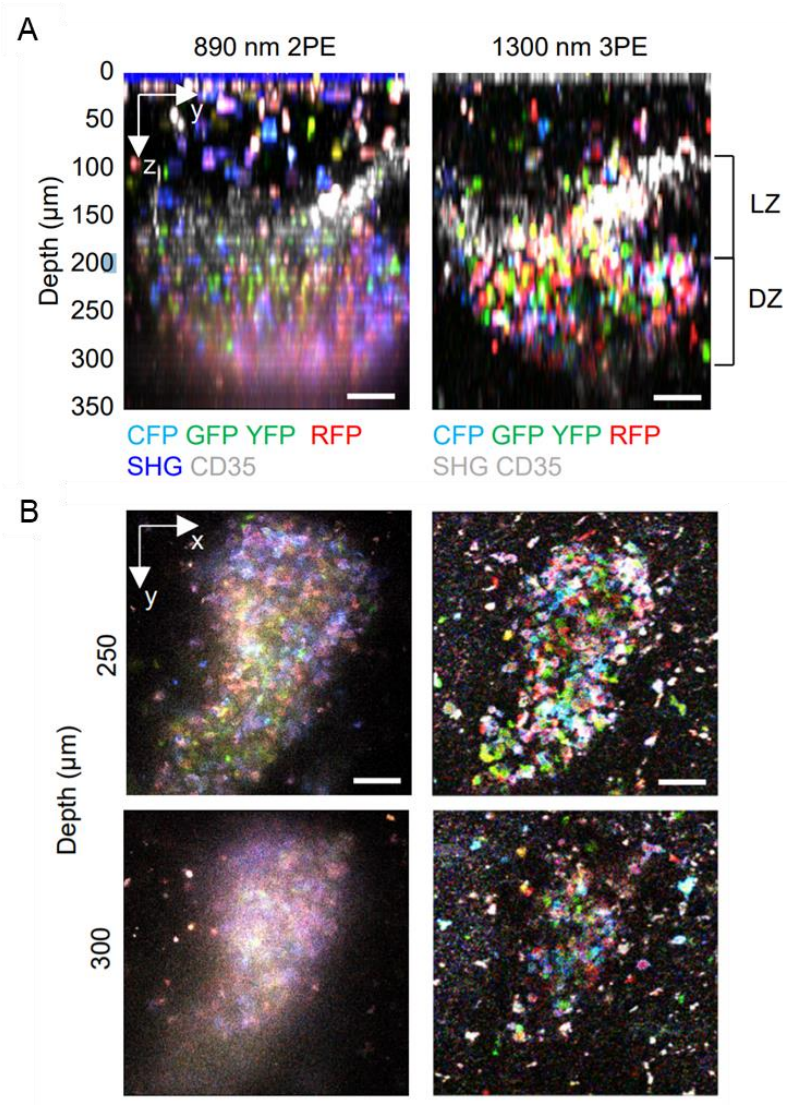

Figure 4-8: *In vivo* 3-photon imaging of GC B cells in confetti mouse lymph node.

A, B) Comparison of GC B cell imaging by 2PM and 3PM. YZ (a) and XY (b) images show multi-color B cells in a GC of the popliteal LN of Cγ1Cre-confetti mouse at 8 days after immunization. LZ is labeled with Alexa Fluor 594-conjugated CD35 antibody. Scale bars, 50 μm.

CHAPTER 5

5.1 Summary

We demonstrated that maleimide polymer end chemistry yielded viable and functional immune organoids over vinylsulfone and acrylate end groups (Chapter 0). We showed that ECM and stromal cells in organoids affect lymphoma drug response and BCR signaling (Chapter CHAPTER 3). We showed that particle-based presentation of antigen to B cells in organoids improved BCR antigen specificity (Chapter **Error! Reference source not found.**). We showed that immunomodulatory nanogels boost germinal response *in vivo* and *ex vivo* with both model and complex antigens.

5.2 Future Outlook

5.2.1 Adding Complexity to ex vivo Models of Lymphoid Tissues

Bridging the gap between *ex vivo* organoids and animal models will allow for more rapid and cost-effective vaccine and therapeutic development. We need to increase the complexity of immune organoids to capture *in vivo* responses *ex vivo*. Next steps include recapitulating spatial organization of lymphoid tissues, adding stromal cells and factors, and further studying mechanical cues.

5.2.2 Spatial Patterning of B Cell Follicles

The current immune organoid model has a mixture of B cells and 40LB stromal cells in an evenly mixed organoid. However, germinal centers are divided into dark zones, where B cells undergo proliferation and somatic hypermutation of the antibody variable region genes, and light zones, where B cells compete for binding to antigen on follicular dendritic cells. CXCL12-expressing and

CXCL13-expressing stromal cells maintain the architecture of these germinal center compartments. Spatially homogenous germinal centers limited interactions between B cells and Tfh cells, which reduced GC output and affinity maturation compared to spatially segregated germinal centers[119]. Future studies can show how spatial patterning of LZ and DZ *ex vivo* affects GC output and affinity maturation.

5.2.3 Cell Migration in Germinal Centers

Stromal cells in germinal center dark zone express CXCL12, which facilitates migration of CXCR4-expressing GC B cells. GC B cells with high CXCR4 expression migrate toward the dark zone. When the cells divide, the daughter cells have reduced surface CXCR4, which causes migration into the light zone. FDCs present antigen to GC B cells in the light zone and provide survival signals to cells with high affinity to antigen and apoptotic signals to cells with low affinity to antigen. The cycle of proliferation and checking is essential to forming high-affinity, antigen-specific antibodies. Future work would be to capture this process to further understand affinity maturation. CXC12-expressing stromal cells are difficult to isolate, so microfluidic devices will be used to generate chemokine gradients. GC B cells and their daughter cells can be tracked to determine how they divide and move back and forth between dark zones and light zones. Patterning of CXCL12 will create limited spaces of CXCL12 that B cells with CXCR4 can interact with, creating competition for CXCL12 between $CXCR4^{hi}$ and $CXCR4^{lo}$ GC B cells.

5.2.4 Incorporating Follicular Dendritic Cells and Mimics

Due to the low numbers of FDCs in lymphoid tissues (<1% of cells), we have been using FDC mimics to present antigen to GC B cells. We presented antigen on human FDC-like cell line HK.

Murine FDC-like cell lines pFL and FL-Y have been shown to express FDC genes including CD21, FcγRIIB, lymphotoxin β receptor, ICAM-1, VCAM-1, IL-6, and C4[120]. However, these cell lines have different characteristics from primary FDCs. In the last few years, relatively straightforward methods of isolating FDCs from murine or human secondary lymphoid tissues by flow cytometry have been reported[121,122]. The next step in adding stromal support in organoids should be to isolate primary FDCs and add them to the light zone of a GC LZ/DZ microfluidic model.

5.2.5 B Cell Receptor and Mechanical Signaling in Organoids

Materials mimicking secondary lymphoid organ stiffness (2300 ± 1000 Pa) have been shown to be optimal for immune stromal cell function[6]. Fluid flow enhances proliferation of malignant B cells through upregulation of expression of IgM, integrin α4, and integrin β1[8]. We would like to incorporate fluid flow in healthy immune tissue models. GC B cells have been shown to use myosin II contractility and high pulling on BCR forces to regulate BCR binding to antigen[9].

5.2.6 B Cell Affinity Separation

To model affinity maturation *ex vivo*, high affinity B cells need to be expanded in organoids. In the absence of survival or apoptotic cues from FDCs, we can remove low affinity B cells and continue culturing high affinity B cells. Microfluidic devices coated with antigen can be used to separate cells with high-affinity and low-affinity BCRs. Future studies aim to use fluid flow to modulate detachment force in microfluidic devices. We can also use microfluidic devices to study how B cells distinguish between high and low affinity binding to antigen. B cell contractility helps separate high and low affinity BCRs by mechanically testing the strength of antigen binding[11]. The

separation device can also be used to study antigen affinity as a function of cell type.

APPENDIX

A.1 Lymphoma Migration via Chemotaxis

Antibodies are routinely formed in vertebrates in response to infections, vaccines, or autoimmune disorders. *Ex vivo* high-affinity antibodies used as therapeutic agents are developed from fused hybridoma models, directly from animal models, genetic engineering of bacteriophages, or cloning antibodies from single antigen-specific human B cells. Yet, these processes cannot explain immune reactions and host-pathogen interactions. There are no mammalian, *ex vivo* lymphoid tissue-like technologies to understand antibody formation dynamics, generate human antibodies, or test efficacy of candidate vaccines. Here we incorporate stromal-specific chemokine gradients in 3D *ex vivo* immune organoids on a microfluidic chip to capture germinal center (GC) B cell dynamics.

FDCs express CXCL13 to recruit B cells to GCs. CXCL12-expressing reticular cells (CRCs) support GC B cells in the dark zone and facilitate migration from light to dark zone in the GC recycling process that produces high-affinity antibodies. CRCs are not easily isolated, therefore we have engineered a CXCL12 concentration gradient on chip to incorporate the chemotaxis effect of CXCL12 on GC B cells (Figure A-1). Devices were fabricated from polydimethylsiloxane (PDMS) bonded to glass microscope slides. The center channel was filled with a hydrogel containing B cells. The top channel was filled with media containing CXCL12, and the bottom channel was filled with media only. Gradient formation on chip was verified through images of dextran-FITC diffusing through PEG hydrogels (Figure A-2). 5 kDa and 10 kDa dextran-FITC were chosen because murine CXCL12 (7.9 kDa) falls between those two sizes. Both 5 kDa and 10 kDa dextran-FITC maintained a concentration gradient after 4 hours, whereas food dye, which is

only about 0.5-1 kDa, was evenly diffused after 4 hours. Murine lymphoma WEHI-231 cells, which migrate in response to CXCL12, were seeded in a PEG-filled microfluidic channel, stimulated with a CXCL12 gradient, imaged, and quantified in high and low CXCL12 concentration zones (Figure A-3). WEHI cells migrated into the CXCL12 media channel but did not migrate into the media only channel.

A.2 Materials and Methods

Microfluidic Device Fabrication

PDMS (Sylgard) base was mixed with crosslinker at a 1:10 ratio, desiccated, poured over microfluidic mold, and baked at 60°C for 2 hrs. Devices were cut and holes were punched for fluidic and hydrogel inlets and outlets. Devices were bonded to clean microscope slides using oxygen plasma (Harrick).

Gradient Formation in Microfluidic Device

7.5% w/v PEG-VS hydrogels were formed by mixing PEG-VS with VPM/DTT crosslinkers and injected into central channel of the microfluidic device. Devices were incubated at 37°C for 15 minutes. Media containing dextran-FITC (or red food dye) was injected into the top fluidic channel, and media only (or media containing blue food dye) was injected into the bottom fluidic channel.

B Cell Migration in Microfluidic Device

WEHI-231 cells stained with CellTracker Green (Thermo Fisher) were mixed into hydrogel mixture and injected to the central channel in the microfluidic device. Devices were incubated at

37°C for 15 minutes. Media containing CXCL12 was injected in one fluidic channel, and media only was injected in the other fluidic channel.

Imaging Analysis

Bright-field images for food dye diffusion were taken on an EVOS XL Core microscope. Fluorescence images were taken on a Nikon TE2000U and analyzed on ImageJ.

A.3 Figures

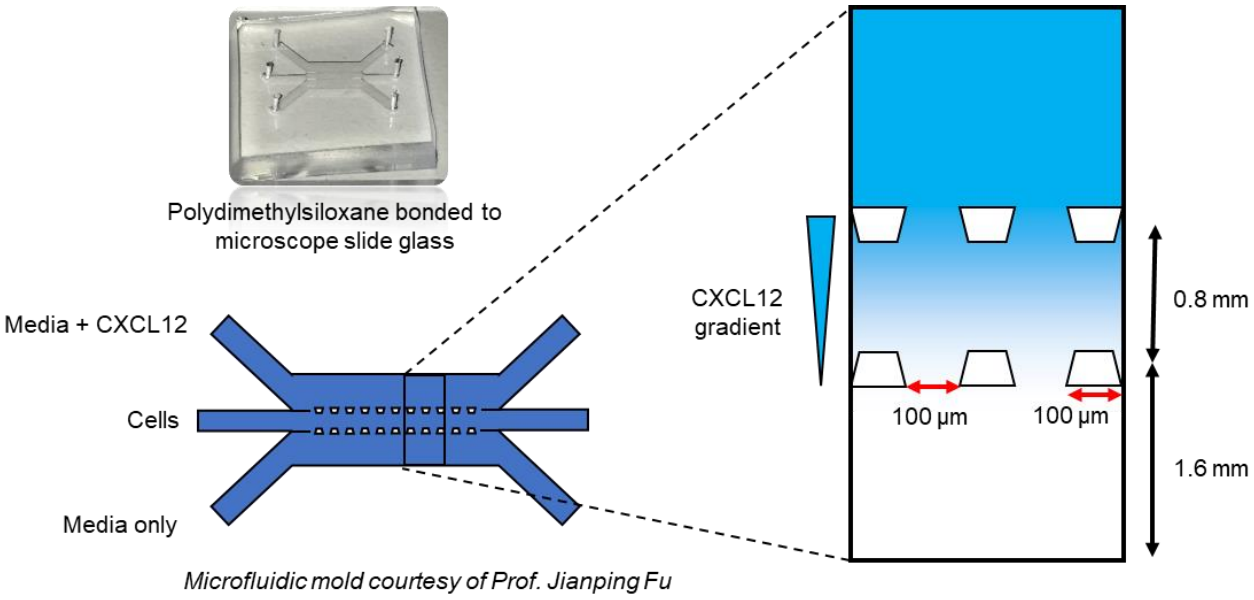

Figure A-1: Microfluidic device for gradient formation in 3D hydrogel.

Microfluidic device is fabricated from PDMS bonded to microscope slide glass.

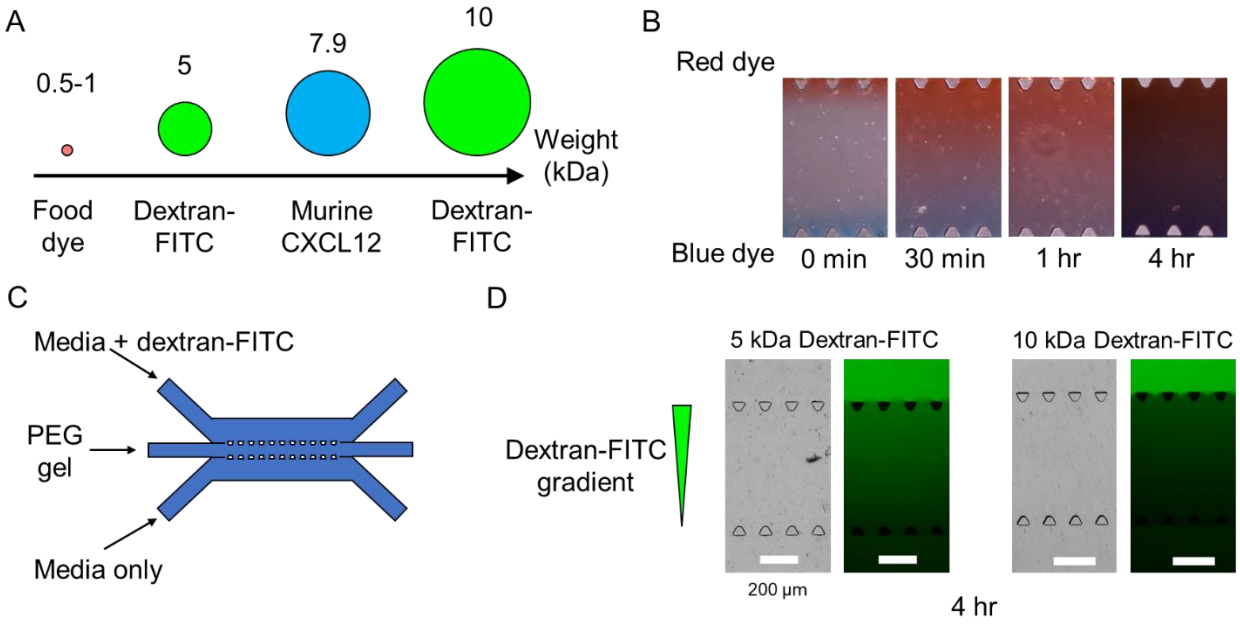

Figure A-2: Gradient formation in hydrogel channel in microfluidic device.

A) Size of dyes and particles relative to chemokine CXCL12.

B) Diffusion of food dye in PEG gel over time.

C) Schematic of microfluidic device with dextran-FITC.

D) Dextran-FITC concentration gradient after 4 hours in device.

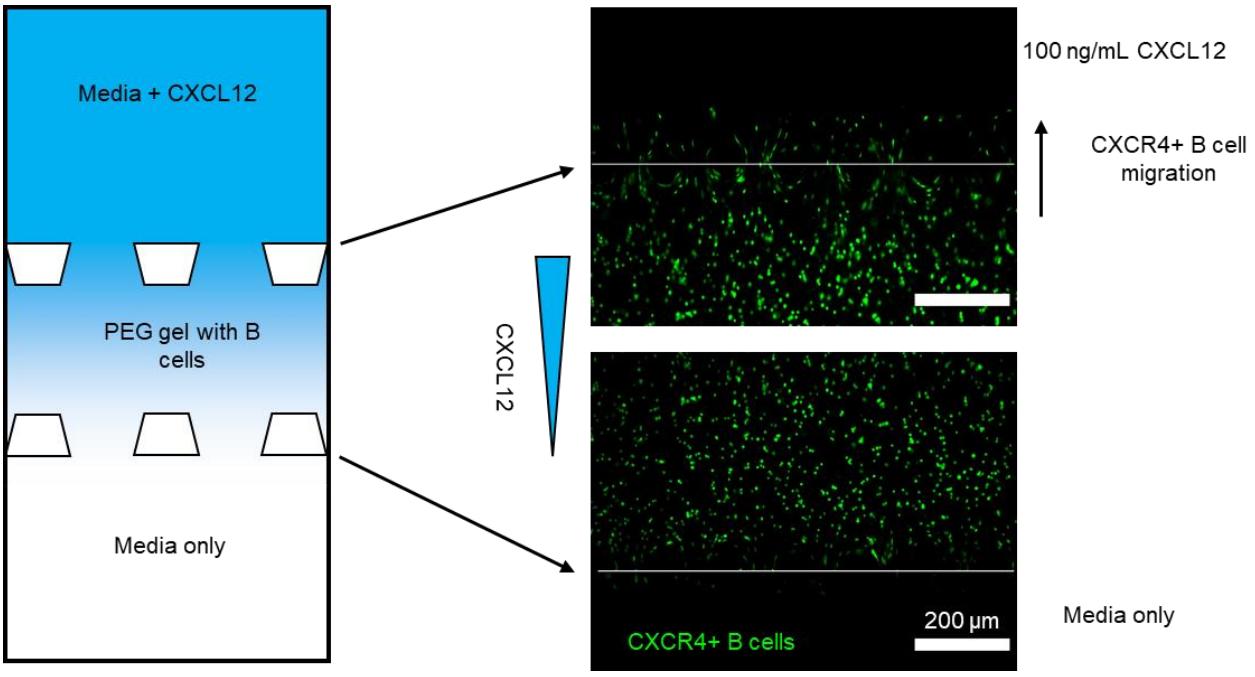

Figure A-3: WEHI-231 migration in 3D hydrogel with CXCL12 gradient.

CXCL12 concentration is high at the top of the channel and low at the bottom of the channel. White line denotes the outer edge of the pillars holding the PEG gel in the central channel.

REFERENCES

1. Dörner, T. & Radbruch, A. Antibodies and B Cell Memory in Viral Immunity. *Immunity* **27**, 384–392 (2007).
2. Mackay, F. & Browning, J. L. BAFF: A fundamental survival factor for B cells. *Nature Reviews Immunology* vol. 2 465–475 (2002).
3. Allen, C. D. C. *et al.* Germinal center dark and light zone organization is mediated by CXCR4 and CXCR5. *Nat. Immunol.* **5**, 943–952 (2004).
4. Nojima, T. *et al.* In-vitro derived germinal centre B cells differentially generate memory B or plasma cells in vivo. *Nat. Commun.* **2**, 465 (2011).
5. Roh, K. H. *et al.* A synthetic stroma-free germinal center niche for efficient generation of humoral immunity ex vivo. *Biomaterials* **164**, 106–120 (2018).
6. Purwada, A. *et al.* Ex vivo engineered immune organoids for controlled germinal center reactions. *Biomaterials* **63**, 24–34 (2015).
7. Purwada, A. *et al.* Ex vivo synthetic immune tissues with T cell signals for differentiating antigen-specific, high affinity germinal center B cells. *Biomaterials* **198**, 27–36 (2019).
8. Apoorva, F. *et al.* How Biophysical Forces Regulate Human B Cell Lymphomas. *Cell Rep.* **23**, 499–511 (2018).
9. Nowosad, C. R., Spillane, K. M. & Tolar, P. Germinal center B cells recognize antigen through a specialized immune synapse architecture. *Nat. Immunol.* **17**, 870–877 (2016).
10. Kwak, K. *et al.* Intrinsic properties of human germinal center B cells set antigen affinity thresholds. *Sci. Immunol.* **3**, (2018).
11. Natkanski, E. *et al.* B cells use mechanical energy to discriminate antigen affinities. *Science (80-.).* **340**, 1587–1590 (2013).
12. Kim, H. S., Zhang, X. & Choi, Y. S. Activation and proliferation of follicular dendritic cell-like cells by activated T lymphocytes. *J. Immunol.* **153**, 2951–2961 (1994).
13. Oelke, M. *et al.* Ex vivo induction and expansion of antigen-specific cytotoxic T cells by HLA-Ig–coated artificial antigen-presenting cells. *Nat. Med. 2003 95* **9**, 619–625 (2003).
14. Medzhitov, R. Toll-like receptors and innate immunity. *Nat. Rev. Immunol. 2001 12* **1**, 135–145 (2001).
15. Hayashi, F. *et al.* The innate immune response to bacterial flagellin is mediated by Toll-like receptor 5. *Nature* **410**, 1099–1103 (2001).
16. Oliveira-Nascimento, L., Massari, P. & Wetzler, L. M. The role of TLR2 ininfection and immunity. *Frontiers in Immunology* vol. 3 (2012).
17. Panda, A. *et al.* Age-Associated Decrease in TLR Function in Primary Human Dendritic Cells Predicts Influenza Vaccine Response. *J. Immunol.* **184**, 2518–2527 (2010).
18. Grohskopf, L. A. *et al.* Prevention and Control of Seasonal Influenza with Vaccines: Recommendations of the Advisory Committee on Immunization Practices, United States, 2021–22 Influenza Season. *MMWR Recomm. Reports* **70**, 1–32 (2021).

19. Jiang, H., Wang, Q. & Sun, X. Lymph node targeting strategies to improve vaccination efficacy. *J. Control. Release* **267**, 47–56 (2017).

20. Kanekiyo, M. *et al.* Self-assembling influenza nanoparticle vaccines elicit broadly neutralizing H1N1 antibodies. *Nature* **499**, 102–106 (2013).

21. Yassine, H. M. *et al.* Hemagglutinin-stem nanoparticles generate heterosubtypic influenza protection. *Nat. Med.* **21**, 1065–1070 (2015).

22. Ross, K. *et al.* Combination Nanovaccine Demonstrates Synergistic Enhancement in Efficacy against Influenza. *ACS Biomater. Sci. Eng.* **2**, 368–374 (2016).

23. Ross, K. *et al.* Single dose combination nanovaccine provides protection against influenza A virus in young and aged mice. *Biomater. Sci.* **7**, 809–821 (2019).

24. Kool, M. *et al.* Alum adjuvant boosts adaptive immunity by inducing uric acid and activating inflammatory dendritic cells. *J. Exp. Med.* **205**, 869–882 (2008).

25. Adams, S. *et al.* Immunization of Malignant Melanoma Patients with Full-Length NY-ESO-1 Protein Using TLR7 Agonist Imiquimod as Vaccine Adjuvant. *J. Immunol.* **181**, 776–784 (2008).

26. Nava-Parada, P., Forni, G., Knutson, K. L., Pease, L. R. & Celis, E. Peptide Vaccine Given with a Toll-Like Receptor Agonist Is Effective for the Treatment and Prevention of Spontaneous Breast Tumors. *Cancer Res.* **67**, 1326–1334 (2007).

27. Kuai, R. *et al.* Dual TLR agonist nanodiscs as a strong adjuvant system for vaccines and immunotherapy. *J. Control. Release* **282**, 131–139 (2018).

28. Feng, Y. *et al.* A toll-like receptor agonist mimicking microbial signal to generate tumor-suppressive macrophages. *Nat. Commun. 2019 101* **10**, 1–14 (2019).

29. Rynkiewicz, D. *et al.* Marked enhancement of the immune response to BioThrax® (Anthrax Vaccine Adsorbed) by the TLR9 agonist CPG 7909 in healthy volunteers. *Vaccine* **29**, 6313–6320 (2011).

30. Wiley, S. R. *et al.* Targeting TLRs Expands the Antibody Repertoire in Response to a Malaria Vaccine. *Sci. Transl. Med.* **3**, (2011).

31. Bargieri, D. Y. *et al.* New malaria vaccine candidates based on the Plasmodium vivax Merozoite Surface Protein-1 and the TLR-5 agonist Salmonella Typhimurium FliC flagellin. *Vaccine* **26**, 6132–6142 (2008).

32. Orr, M. T. *et al.* A dual TLR agonist adjuvant enhances the immunogenicity and protective efficacy of the tuberculosis vaccine antigen ID93. *PLoS One* **9**, e83884 (2014).

33. Cooper, C. L. *et al.* CPG 7909, an immunostimulatory TLR9 agonist oligodeoxynucleotide, as adjuvant to Engerix-B® HBV vaccine in healthy adults: A double-blind phase I/II study. *J. Clin. Immunol.* **24**, 693–701 (2004).

34. Hong, B. *et al.* A Super TLR Agonist to Improve Efficacy of Dendritic Cell Vaccine in Induction of Anti-HCV Immunity. *PLoS One* **7**, e48614 (2012).

35. Lynn, G. M. *et al.* In vivo characterization of the physicochemical properties of polymer-linked TLR agonists that enhance vaccine immunogenicity. *Nat. Biotechnol. 2015 3311* **33**, 1201–1210 (2015).

36. Heesters, B. A., van der Poel, C. E., Das, A. & Carroll, M. C. Antigen Presentation to B Cells. *Trends in Immunology* vol. 37 844–854 (2016).

37. Béguelin, W. *et al.* EZH2 enables germinal centre formation through epigenetic silencing of CDKN1A and an Rb-E2F1 feedback loop. *Nat. Commun.* **8**, 1–16 (2017).

38. Purwada, A. & Singh, A. Immuno-engineered organoids for regulating the kinetics of B-cell development and antibody production. *Nat. Protoc.* **12**, 168–182 (2017).

39. Kim, S., Shah, S. B., Graney, P. L. & Singh, A. Multiscale engineering of immune cells and lymphoid organs. *Nature Reviews Materials* vol. 4 355–378 (2019).

40. Bian, L., Guvendiren, M., Mauck, R. L. & Burdick, J. A. Hydrogels that mimic developmentally relevant matrix and N-cadherin interactions enhance MSC chondrogenesis. *Proc. Natl. Acad. Sci. U. S. A.* **110**, 10117–10122 (2013).

41. McKinnon, D. D., Domaille, D. W., Cha, J. N. & Anseth, K. S. Biophysically defined and cytocompatible covalently adaptable networks as viscoelastic 3d cell culture systems. *Adv. Mater.* **26**, 865–872 (2014).

42. Grover, G. N., Lam, J., Nguyen, T. H., Segura, T. & Maynard, H. D. Biocompatible hydrogels by oxime click chemistry. *Biomacromolecules* **13**, 3013–3017 (2012).

43. Boere, K. W. M. *et al.* Biofabrication of reinforced 3D-scaffolds using two-component hydrogels †. *J. Mater. Chem. B* **3**, 9067 (2015).

44. Smith, L. J. *et al.* Diels-Alder Click-Cross-Linked Hydrogels with Increased Reactivity Enable 3D Cell Encapsulation. *Biomacromolecules* **19**, 926–935 (2018).

45. Alge, D. L., Azagarsamy, M. A., Donohue, D. F. & Anseth, K. S. Synthetically tractable click hydrogels for three-dimensional cell culture formed using tetrazine-norbornene chemistry. *Biomacromolecules* **14**, 949–953 (2013).

46. Qin, X. H., Wang, X., Rottmar, M., Nelson, B. J. & Maniura-Weber, K. Near-Infrared Light-Sensitive Polyvinyl Alcohol Hydrogel Photoresist for Spatiotemporal Control of Cell-Instructive 3D Microenvironments. *Adv. Mater.* **30**, 1–7 (2018).

47. Skardal, A. *et al.* A hydrogel bioink toolkit for mimicking native tissue biochemical and mechanical properties in bioprinted tissue constructs. *Acta Biomater.* **25**, 24–34 (2015).

48. Lee, T. T. *et al.* Light-triggered in vivo activation of adhesive peptides regulates cell adhesion, inflammation and vascularization of biomaterials. *Nat. Mater.* **14**, 352–360 (2015).

49. Phelps, E. A. *et al.* Maleimide cross-linked bioactive PEG hydrogel exhibits improved reaction kinetics and cross-linking for cell encapsulation and in situ delivery. *Adv. Mater.* **24**, 64–70 (2012).

50. Phelps, E. A., Headen, D. M., Taylor, W. R., Thulé, P. M. & García, A. J. Vasculogenic bio-synthetic hydrogel for enhancement of pancreatic islet engraftment and function in type 1 diabetes. *Biomaterials* **34**, 4602–4611 (2013).

51. Macdougall, L. J., Pérez-Madrigal, M. M., Arno, M. C. & Dove, A. P. Nonswelling Thiol-Yne Cross-Linked Hydrogel Materials as Cytocompatible Soft Tissue Scaffolds. *Biomacromolecules* **19**, 1378–1388 (2018).

52. Truong, V. X., Ablett, M. P., Richardson, S. M., Hoyland, J. A. & Dove, A. P. Simultaneous Orthogonal Dual-Click Approach to Tough, in-Situ-Forming Hydrogels for Cell Encapsulation. *J. Am. Chem. Soc* **137**, 12 (2015).

53. Truong, V. X., Tsang, K. M. & Forsythe, J. S. Nonswelling Click-Cross-Linked Gelatin and PEG Hydrogels with Tunable Properties Using Pluronic Linkers. *Biomacromolecules* **18**, 757–766 (2017).

54. Huynh, C. T., Liu, F., Cheng, Y., Coughlin, K. A. & Alsberg, E. Thiol-Epoxy 'click' Chemistry to Engineer Cytocompatible PEG-Based Hydrogel for siRNA-Mediated Osteogenesis of hMSCs. *ACS Appl. Mater. Interfaces* **10**, 25936–25942 (2018).

55. Paez, J. I. *et al.* Thiol-Methylsulfone-Based Hydrogels for 3D Cell Encapsulation. *Cite This ACS Appl. Mater. Interfaces* **12**, 8072 (2020).

56. Rydholm, A. E., Bowman, C. N. & Anseth, K. S. Degradable thiol-acrylate photopolymers: polymerization and degradation behavior of an in situ forming biomaterial. *Biomaterials* **26**, 4495–4506 (2005).

57. Clark, A. Y. *et al.* Integrin-specific hydrogels modulate transplanted human bone marrow-derived mesenchymal stem cell survival, engraftment, and reparative activities. *Nat. Commun.* **11**, (2020).

58. Cruz-Acuña, R. *et al.* Synthetic hydrogels for human intestinal organoid generation and colonic wound repair. *Nat. Cell Biol.* **19**, 1326–1335 (2017).

59. Gjorevski, N. *et al.* Designer matrices for intestinal stem cell and organoid culture. *Nature* **539**, 560–564 (2016).

60. Raeber, G. P., Lutolf, M. P. & Hubbell, J. A. Molecularly engineered PEG hydrogels: A novel model system for proteolytically mediated cell migration. *Biophys. J.* **89**, 1374–1388 (2005).

61. Kraehenbuehl, T. P. *et al.* Three-dimensional extracellular matrix-directed cardioprogenitor differentiation: Systematic modulation of a synthetic cell-responsive PEG-hydrogel. *Biomaterials* **29**, 2757–2766 (2008).

62. Park, Y., Lutolf, M. P., Hubbell, J. A., Hunziker, E. B. & Wong, M. Bovine Primary Chondrocyte Culture in Synthetic Matrix Metalloproteinase-Sensitive Poly(ethylene glycol)-Based Hydrogels as a Scaffold for Cartilage Repair. *Tissue Eng.* **10**, 515–522 (2004).

63. Goldberg, M. S. Improving cancer immunotherapy through nanotechnology. *Nature Reviews Cancer* vol. 19 587–602 (2019).

64. Polini, A. *et al.* Towards the development of human immune-system-on-a-chip platforms. *Drug Discov. Today* **24**, 517–525 (2019).

65. Hao, Z. *et al.* Fas Receptor Expression in Germinal-Center B Cells Is Essential for T and B Lymphocyte Homeostasis. *Immunity* **29**, 615–627 (2008).

66. Cyster, J. G. B cell follicles and antigen encounters of the third kind. *Nature Immunology* vol. 11 989–996 (2010).

67. Knight, C. G. *et al.* Identification in Collagen Type I of an Integrin α2β1-binding Site

Containing an Essential GER Sequence *. *J. Biol. Chem.* **273**, 33287–33294 (1998).

68. Zeltz, C. & Gullberg, D. The integrin–collagen connection – a glue for tissue repair? *J. Cell Sci.* **129**, 653–664 (2016).

69. Massia, S. P. & Hubbell, J. A. Vascular endothelial cell adhesion and spreading promoted by the peptide REDV of the IIICS region of plasma fibronectin is mediated by integrin α4β1. *J. Biol. Chem.* **267**, 14019–14026 (1992).

70. Arnaout, M. A., Mahalingam, B. & Xiong, J. P. Integrin structure, allostery, and bidirectional signaling. *Annual Review of Cell and Developmental Biology* vol. 21 381–410 (2005).

71. Bellis, S. L. Advantages of RGD peptides for directing cell association with biomaterials. *Biomaterials* **32**, 4205–4210 (2011).

72. Purwada, A., Shah, S. B., Beguelin, W., Melnick, A. M. & Singh, A. Modular Immune Organoids with Integrin Ligand Specificity Differentially Regulate Ex Vivo B Cell Activation. *ACS Biomater. Sci. Eng.* **3**, 214–225 (2017).

73. Phelan, J. D. *et al.* A multiprotein supercomplex controlling oncogenic signalling in lymphoma. *Nature* 1 (2018) doi:10.1038/s41586-018-0290-0.

74. Chapuy, B. *et al.* Molecular subtypes of diffuse large B cell lymphoma are associated with distinct pathogenic mechanisms and outcomes. *Nat. Med. 2018 245* **24**, 679–690 (2018).

75. Sinha, R., Nastoupil, L. J. & Flowers, C. R. Treatment strategies for patients with diffuse large B-cell lymphoma: past, present, and future. *Blood Lymphat. Cancer Targets Ther.* **2**, 87–98 (2012).

76. Roschewski, M., Staudt, L. M. & Wilson, W. H. Diffuse large B-cell lymphoma—treatment approaches in the molecular era. *Nat. Rev. Clin. Oncol. 2013 111* **11**, 12–23 (2013).

77. Lenz, G. *et al.* Oncogenic CARD11 mutations in human diffuse large B cell lymphoma. *Science (80-.).* **319**, 1676–1679 (2008).

78. Schmitz, R. *et al.* Genetics and Pathogenesis of Diffuse Large B-Cell Lymphoma. *N. Engl. J. Med.* **378**, 1396–1407 (2018).

79. Wilson, W. H. *et al.* Targeting B cell receptor signaling with ibrutinib in diffuse large B cell lymphoma. *Nat. Med. 2015 218* **21**, 922–926 (2015).

80. Reddy, A. *et al.* Genetic and Functional Drivers of Diffuse Large B Cell Lymphoma. *Cell* **171**, 481-494.e15 (2017).

81. Wright, G. W. *et al.* A Probabilistic Classification Tool for Genetic Subtypes of Diffuse Large B Cell Lymphoma with Therapeutic Implications. *Cancer Cell* **37**, 551-568.e14 (2020).

82. Fontan, L. *et al.* Identification of MALT1 feedback mechanisms enables rational design of potent antilymphoma regimens for ABC-DLBCL. *Blood* **137**, 788–800 (2021).

83. Young, R. M. & Staudt, L. M. Targeting pathological B cell receptor signalling in lymphoid malignancies. *Nat. Rev. Drug Discov. 2013 123* **12**, 229–243 (2013).

84. Sun, L., Deng, L., Ea, C. K., Xia, Z. P. & Chen, Z. J. The TRAF6 Ubiquitin Ligase and

TAK1 Kinase Mediate IKK Activation by BCL10 and MALT1 in T Lymphocytes. *Mol. Cell* **14**, 289–301 (2004).

85. Hailfinger, S. *et al.* Malt1-dependent RelB cleavage promotes canonical NF-κB activation in lymphocytes and lymphoma cell lines. *Proc. Natl. Acad. Sci.* **108**, 14596–14601 (2011).

86. Fontan, L. *et al.* MALT1 Small Molecule Inhibitors Specifically Suppress ABC-DLBCL In Vitro and In Vivo. *Cancer Cell* **22**, 812–824 (2012).

87. Fontán, L. *et al.* Specific covalent inhibition of MALT1 paracaspase suppresses B cell lymphoma growth. *J. Clin. Invest.* **128**, 4397–4412 (2018).

88. Nagel, D. *et al.* Pharmacologic Inhibition of MALT1 Protease by Phenothiazines as a Therapeutic Approach for the Treatment of Aggressive ABC-DLBCL. *Cancer Cell* **22**, 825–837 (2012).

89. Scott, D. W. & Gascoyne, R. D. The tumour microenvironment in B cell lymphomas. *Nature Reviews Cancer* vol. 14 517–534 (2014).

90. Havranek, O. *et al.* Tonic B-cell receptor signaling in diffuse large B-cell lymphoma. *Blood* **130**, 995–1006 (2017).

91. Lu, Y. *et al.* Src Family Protein-tyrosine Kinases Alter the Function of PTEN to Regulate Phosphatidylinositol 3-Kinase/AKT Cascades *. *J. Biol. Chem.* **278**, 40057–40066 (2003).

92. Béguelin, W. *et al.* IL10 receptor is a novel therapeutic target in DLBCLs. *Leukemia* **29**, 1684–1694 (2015).

93. Wang, X. *et al.* Follicular dendritic cells help establish follicle identity and promote B cell retention in germinal centers. *J. Exp. Med.* **208**, 2497–2510 (2011).

94. Pedersen, H. K. *et al.* Human gut microbes impact host serum metabolome and insulin sensitivity. *Nat. 2016 5357612* **535**, 376–381 (2016).

95. Lusis, A. J., Attie, A. D. & Reue, K. Metabolic syndrome: from epidemiology to systems biology. *Nat. Rev. Genet. 2008 911* **9**, 819–830 (2008).

96. Grundy, S. M. *et al.* Diagnosis and Management of the Metabolic Syndrome. *Circulation* **112**, 2735–2752 (2005).

97. Huang, P. L. A comprehensive definition for metabolic syndrome. *Dis. Model. Mech.* **2**, 231–237 (2009).

98. Ussar, S. *et al.* Interactions between Gut Microbiota, Host Genetics and Diet Modulate the Predisposition to Obesity and Metabolic Syndrome. *Cell Metab.* **22**, 516–530 (2015).

99. Le Chatelier, E. *et al.* Richness of human gut microbiome correlates with metabolic markers. *Nat. 2013 5007464* **500**, 541–546 (2013).

100. Sheridan, P. A. *et al.* Obesity is associated with impaired immune response to influenza vaccination in humans. *Int. J. Obes.* **36**, 1072–1077 (2012).

101. Vijay-Kumar, M. *et al.* Metabolie syndrome and altered gut microbiota in mice lacking toll-like receptor 5. *Science (80-.).* **328**, 228–231 (2010).

102. Oh, J. Z. *et al.* TLR5-mediated sensing of gut microbiota is necessary for antibody responses to seasonal influenza vaccination. *Immunity* **41**, 478–492 (2014).

103. Kasturi, S. P. *et al.* Programming the magnitude and persistence of antibody responses with innate immunity. *Nat. 2011 4707335* **470**, 543–547 (2011).

104. Singh, A. *et al.* Efficient Modulation of T-cell Response by Dual-mode, Single-carrier Delivery of Cytokine-targeted siRNA and DNA Vaccine to Antigen-presenting Cells. *Mol. Ther.* **16**, 2011–2021 (2008).

105. Gitlin, A. D. *et al.* T cell help controls the speed of the cell cycle in germinal center B cells. *Science (80-.).* **349**, 643–646 (2015).

106. Seong, S. Y. & Matzinger, P. Hydrophobicity: An ancient damage-associated molecular pattern that initiates innate immune responses. *Nature Reviews Immunology* vol. 4 469–478 (2004).

107. Jin, M. S. *et al.* Crystal Structure of the TLR1-TLR2 Heterodimer Induced by Binding of a Tri-Acylated Lipopeptide. *Cell* **130**, 1071–1082 (2007).

108. Guan, Y., Omueti-Ayoade, K., Mutha, S. K., Hergenrother, P. J. & Tapping, R. I. Identification of Novel Synthetic Toll-like Receptor 2 Agonists by High Throughput Screening *. *J. Biol. Chem.* **285**, 23755–23762 (2010).

109. Park, B. S. & Lee, J.-O. Recognition of lipopolysaccharide pattern by TLR4 complexes. *Exp. Mol. Med. 2013 4512* **45**, e66–e66 (2013).

110. Jin, M. S. & Lee, J. O. Structures of the Toll-like Receptor Family and Its Ligand Complexes. *Immunity* **29**, 182–191 (2008).

111. Brandão, I., Hörmann, N., Jäckel, S. & Reinhardt, C. TLR5 expression in the small intestine depends on the adaptors MyD88 and TRIF, but is independent of the enteric microbiota. *https://doi.org/10.1080/19490976.2015.1034417* **6**, 202–206 (2015).

112. Schudel, A., Francis, D. M. & Thomas, S. N. Material design for lymph node drug delivery. *Nature Reviews Materials* vol. 4 415–428 (2019).

113. Casola, S. *et al.* Tracking germinal center B cells expressing germ-line immunoglobulin γ1 transcripts by conditional gene targeting. *Proc. Natl. Acad. Sci.* **103**, 7396–7401 (2006).

114. Livet, J. *et al.* Transgenic strategies for combinatorial expression of fluorescent proteins in the nervous system. *Nat. 2007 4507166* **450**, 56–62 (2007).

115. Tas, J. M. J. *et al.* Visualizing antibody affinity maturation in germinal centers. *Science (80-.).* **351**, 1048–1054 (2016).

116. Lewis, S. M., Williams, A. & Eisenbarth, S. C. Structure and function of the immune system in the spleen. *Sci. Immunol.* **4**, (2019).

117. Zhang, T., Al-Alwan, M. & Marshall, A. J. The Pleckstrin Homology Domain Adaptor Protein Bam32/DAPP1 Is Required for Germinal Center Progression. *J. Immunol.* **184**, 164–172 (2010).

118. Sage, P. T., Tan, C. L., Freeman, G. J., Haigis, M. & Sharpe, A. H. Defective TFH Cell Function and Increased TFR Cells Contribute to Defective Antibody Production in Aging. *Cell Rep.* **12**, 163–171 (2015).

119. Pikor, N. B. *et al.* Remodeling of light and dark zone follicular dendritic cells governs germinal center responses. *Nat. Immunol.* **21**, 649–659 (2020).

120. Nishikawa, Y. *et al.* Establishment of Lymphotoxin β Receptor Signaling-Dependent Cell Lines with Follicular Dendritic Cell Phenotypes from Mouse Lymph Nodes. *J. Immunol.* **177**, 5204–5214 (2006).

121. Heesters, B. A., Poel, C. E. Van der & Carroll, M. C. Follicular Dendritic Cell Isolation and Loading of Immune Complexes. *Methods Mol. Biol.* **1623**, 105–112 (2017).

122. Shikh, M. E. M. El, Sayed, R. El & Pitzalis, C. Isolation and Characterization of Mouse and Human Follicular Dendritic Cells. *Methods Mol. Biol.* **1623**, 113–123 (2017).

123. Graney, P. L. *et al.* Organoid Polymer Functionality and Mode of Klebsiella pneumoniae Membrane Antigen Presentation Regulates Ex Vivo Germinal Center Epigenetics in Young and Aged B Cells. *Adv. Funct. Mater.* **30**, 1–16 (2020).

124. Mosquera, M. J. *et al.* Immunomodulatory nanogels overcome restricted immunity in a murine model of gut microbiome–mediated metabolic syndrome. *Sci. Adv.* **5**, eaav9788 (2019).